







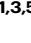
# An ex vivo uterine system captures implantation, embryogenesis, and trophoblast invasion via maternal-embryonic signaling

Received: 21 November 2024

Accepted: 21 May 2025

Published online: 01 July 2025



Takehiro Hiraoka <sup>1,2</sup>✉, Shizu Aikawa <sup>2</sup>, Daisuke Mashiko <sup>1</sup>,  
Tatsuya Nakagawa <sup>1,3</sup>, Hiroki Shirai<sup>4</sup>, Yasushi Hirota <sup>2</sup>, Hiroshi Kimura <sup>4</sup> &  
Masahito Ikawa <sup>1,3,5,6,7</sup>✉

Embryo implantation remains challenging to study because of its inaccessibility in situ despite its essentiality and clinical significance. Although recent studies on long-term culture of authentic and model embryos have provided significant advances in elucidating embryogenesis in vitro, they, without the uterus, cannot genuinely replicate implantation. Here, we have recapitulated bona fide implantation ex vivo at more than 90% efficiency followed by embryogenesis and trophoblast invasion using authentic mouse embryos and uterine tissue. We utilized air-liquid interface culture method with originally developed devices manufactured with polydimethylsiloxane. Notably, the system replicated the robust induction of a maternal implantation regulator COX-2 at the attachment interface, which was accompanied by trophoblastic AKT activation, suggesting a possible signaling that mediates maternal COX-2 and embryonic AKT1 that accelerates implantation. By expanding the ex vivo findings, embryonic AKT1 transduction ameliorated defective implantation of uterine origin by a COX-2 inhibitor in vivo. The system, proposing a potentially standard platform of embryogenesis, offers a concise, reproducible, and scalable screening system, suggesting significant implications for developmental biology and therapeutic strategies for recurrent implantation failure in assisted reproductive technology.

Embryo implantation, a process including embryonic attachment and trophoblast invasion into the endometrium, is indispensable for the embryogenesis of mammals. The fact that approximately 50 to 60% of embryos are lost at the time of implantation in assisted reproductive technologies (ART)<sup>1</sup> while the miscarriage rate of successfully

implanted embryos is ~15%<sup>2</sup> implies that implantation is a rate-limiting step in human development. This fact highlights the significance of implantation research, but currently available knowledge is limited. This is because, for example, while fertilization and preimplantation development can be reproduced, observed, and manipulated in vitro,

<sup>1</sup>Research Institute for Microbial Diseases, Osaka University, Osaka, Japan. <sup>2</sup>Department of Obstetrics and Gynecology, Graduate School of Medicine, The University of Tokyo, Tokyo, Japan. <sup>3</sup>Graduate School of Pharmaceutical Sciences, Osaka University, Osaka, Japan. <sup>4</sup>Micro/Nano Technology Center, Tokai University, Kanagawa, Japan. <sup>5</sup>Center for Infectious Disease Education and Research (CiDER), Osaka University, Osaka, Japan. <sup>6</sup>The Institute of Medical Science, The University of Tokyo, Tokyo, Japan. <sup>7</sup>Center for Advanced Modalities and DDS (CAMA-DS), Osaka University, Osaka, Japan.

✉ e-mail: [t\\_hiraoka1985@yahoo.co.jp](mailto:t_hiraoka1985@yahoo.co.jp); [ikawa@biken.osaka-u.ac.jp](mailto:ikawa@biken.osaka-u.ac.jp)

implantation is a spatiotemporally dynamic phenomenon that can only be reproduced *in vivo*, involving a close interplay between embryos and each component of endometrial cells including not only luminal epithelial cells but also stromal cells, glandular epithelial cells, vascular endothelial cells, and immune cells. Implantation-assisting techniques available in current ART only include assisted hatching by the zona punctura incision and frozen-thawed embryo transfer after ovarian stimulation<sup>3</sup>. Unfortunately, none of these have led to a dramatic improvement in implantation efficiency, and none have led to the establishment of groundbreaking treatments such as ICSI (Intra Cytoplasmic Sperm Injection) for fertilization disorder.

Although dramatic progress in basic research on implantation is desirable, basic research on human implantation is intractable due to technical and ethical issues, and this is why attempts have been made to elucidate the molecular and cellular mechanisms of implantation using genetically modified mice. Although this approach is robust in terms of elucidating gene function in implantation, using systemic gene-deficient mice is often not straightforward. For example, systemically deficient mice of STAT3 and Gp130, which are among the major downstream molecules of LIF, exhibit embryonic lethality<sup>4,5</sup>, and systemically deficient mice of LIFR show perinatal lethality<sup>6</sup>, making it impossible to observe the implantation phenotype in adult females. In addition, mice with systemic deficiency of the progesterone receptor are unsuitable for evaluating uterine functions during implantation because they exhibit ovulation defects<sup>7</sup>. Conditional gene knockout (KO), a powerful technique routinely used at present, of the above-mentioned genes has shown that these genes are essential for implantation<sup>8–10</sup>. However, generating conditional KO mice requires more time and effort than generating systemic KO mice. Considering these facts, an *ex vivo* experimental system that faithfully reproduces implantation would facilitate implantation research and benefit future studies using human specimens.

In recent years, advances in long-term embryonic culture methods have been achieved in a series of studies using mouse, bovine, monkey, and human authentic or model embryos derived from stem cells to mimic preimplantation to postimplantation embryonic development<sup>11–15</sup> especially highlighted by stem cell-based human embryogenesis models<sup>16–19</sup>. However, without the uterus, these models cannot replicate embryonic attachment and trophoblast infiltration via embryo-maternal interactions. Developmental cessation at E11 *ex utero* with a lack of placental formation in a previous mouse study<sup>12</sup> suggests a demand for a co-culture system with uterine tissue. Similarly, recent studies have offered several models to study embryo implantation *in vitro/ex vivo*, utilizing hydrogels and endometrial organoids as implantation platforms<sup>20–22</sup>. However, with the lack of whole uterine components that orchestrate implantation *in vivo*, satisfactory recapitulation of embryo implantation has not been achieved.

Here, we present an *ex vivo* system that faithfully replicates the aspects of embryo implantation including embryonic attachment and trophoblast invasion accompanied by embryogenesis on the *ex vivo* uterus, enabled by combining and optimizing the extended embryonic culture and tissue culture methods.

## Results

### Robust induction of implantation by an *ex vivo* uterine system

To replicate authentic embryo implantation *ex vivo*, we focused on uterine tissue culture. Previous studies have demonstrated the advantage of the air-liquid interface (ALI) method in tissue culture primarily on seminiferous tubules<sup>23</sup>. In this study, day post coitum (dpc) 3.75 endometria were isolated and co-cultured with E3.75 blastocysts (Fig. 1A and B) by the ALI method using originally developed devices made of gas-permeable polydimethylsiloxane (PDMS) (Fig. 1C) especially to facilitate delivery of low-soluble oxygen. The fact that the endometrium, with a thickness of ~250  $\mu\text{m}$ , is thicker than seminiferous tubules and possesses tissue polarity of the luminal and stromal

ends led us to assume the gradient of oxygen concentration in the tissue. Because the oxygen gradient may potentially affect the outcomes, the direction of the oxygen supply was changed by the arrangement of the devices and tissues. Concomitantly, several cultural settings were probed to maximize the outcome.

As a result of comprehensive verifications (Supplementary Fig. 1A–G), an optimized condition was found, in which the embryos were fixed on the endometrial luminal epithelium with PDMS ceilings (Fig. 1C, D and E), with oxygen supply, with delivery of medium from the stroma through an agarose gel. In the verifications, the efficiency of oxygen supply was examined by the modulation of the thickness of PDMS<sup>24</sup>, the absence of PDMS, the vertical arrangement of the embryos and endometria, and the usage of glass (Supplementary Fig. 1A and B). Consequently, more than 90% of embryos were rigidly attached to the endometria at 24 h (24 h) with 750  $\mu\text{m}$ -thick PDMS ceilings (Fig. 2A–G). Although the attachment efficiencies were similar between 750  $\mu\text{m}$ -thick and 1500  $\mu\text{m}$ -thick PDMS ceilings, 750  $\mu\text{m}$ -thick PDMS produced slightly better results (95.8 % vs 94.8 %, not significant) and facilitated observation under fluorescent upright microscopes in terms of the transparency and the interference of the objective lens and PDMS. The results of allogeneic co-culture were equivalent to those of autologous co-culture (Supplementary Fig. 1C). Unexpectedly, placing embryos in the liquid phase never allowed attachment (Supplementary Fig. 1A and B). Critically, the medium, named *ex vivo* implantation (EXiM) medium, was developed based on the IVC2 medium containing KSR instead of FCS (FBS)<sup>11</sup>, and the ovarian hormone levels were optimized to the physiological levels of 3 pg/mL for 17 $\beta$ -estradiol and 60 ng/mL for progesterone<sup>8,25</sup>. A higher level of 17 $\beta$ -estradiol severely abrogated embryonic attachment (Supplementary Fig. 1D), and the pregnant mare serum gonadotropin (PMSG)-stimulated endometria before mating also showed impaired embryonic attachment (Supplementary Fig. 1E). Conversely, PMSG-stimulated embryos showed comparable attachment efficiency to that of naturally ovulated embryos (Supplementary Fig. 1F). A brief use of acidified Tyrode's solution (AT) did not affect the results (Supplementary Fig. 1G).

In mice, mural trophoblast (mTE), not polar trophoblast (pTE), attaches to the endometrium<sup>26</sup>. Our *ex vivo* system robustly reproduced mTE attachment at 24 h, as evidenced by the microscopic findings (Fig. 2A–G, and Movie S1) and endometrial epithelial remnants attached on mTE which was similar to E4.5 embryos (Supplementary Fig. 2A). Curiously, autofluorescence was reproducibly detected before PDMS removal in the area of mTE, never of pTE (Supplementary Fig. 2B), suggesting the emergence of certain cellular events in mTE or a certain type of cell death in endometrial epithelial cells<sup>27,28</sup>.

It has been demonstrated that peri- and postimplantation TE shows CDX2 gradation<sup>29,30</sup>, suggesting its differentiation into pTE and mTE. Our systems also replicated the phenomenon (Fig. 2B–G, Movie S1) under differential conditions even without implantation (Supplementary Fig. 3A and B). On the other hand, the number of trophoblast (TE) cells in embryos co-cultured in contact with the endometria but failed to attach (defined in Methods) was significantly higher than that in embryos co-cultured without contact with the endometria (Supplementary Fig. 3C and D). In addition, the TE cell number further increased by the successful attachment to the endometria (Supplementary Fig. 3C and D), consistent with a prior stem cell-based implantation model<sup>31</sup>, indicating the role of implantation for the proliferation of TE, putatively mediated through paracrine factors from the endometria, such as cytokines, growth factors, and lipid mediators, and integrin signals.

### Embryogenesis on *ex vivo* uterus

Persistent coverage with PDMS (Supplementary Fig. 4A) failed to enable further embryonic development after 24 h. Under this PDMS-

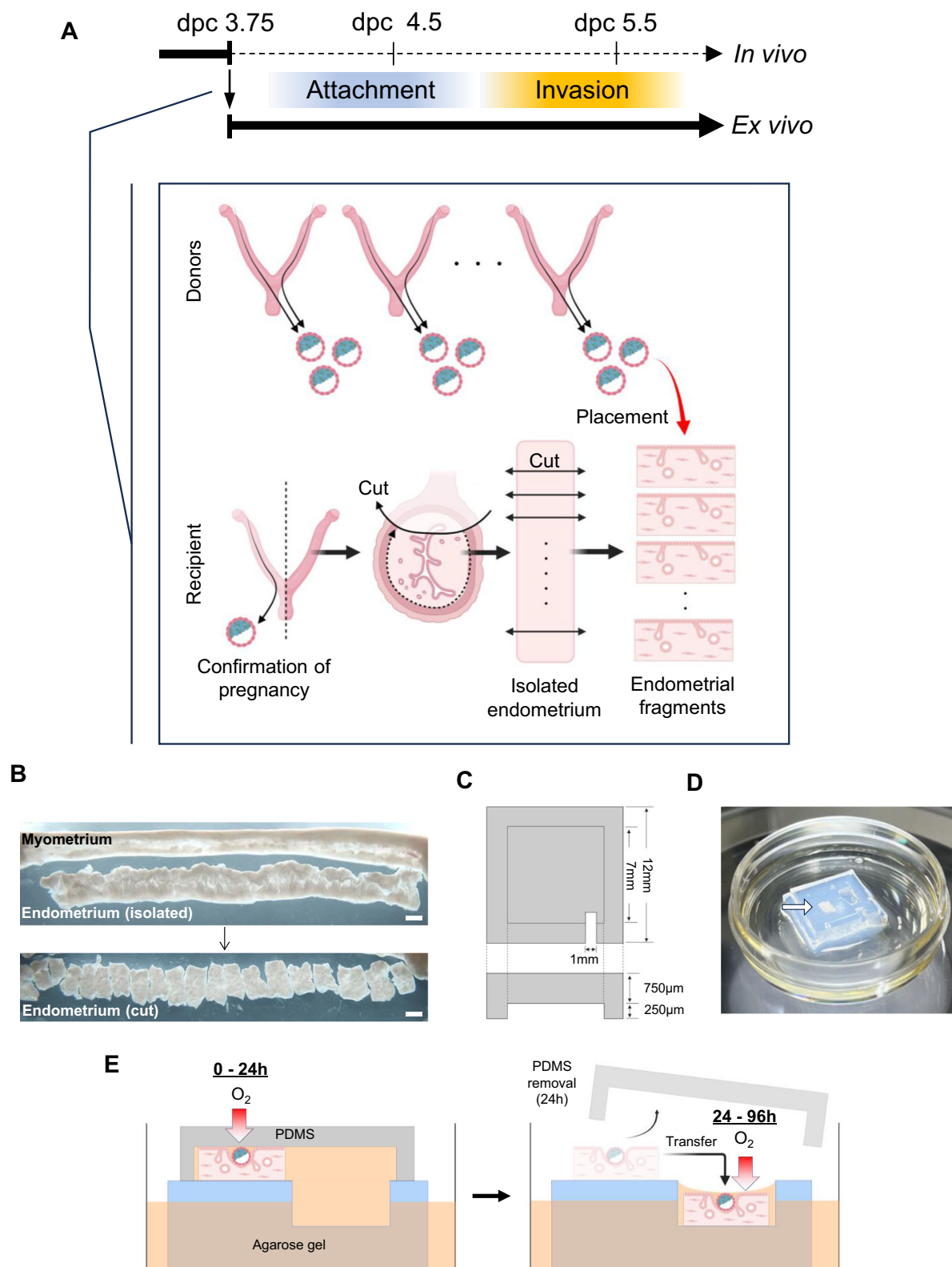
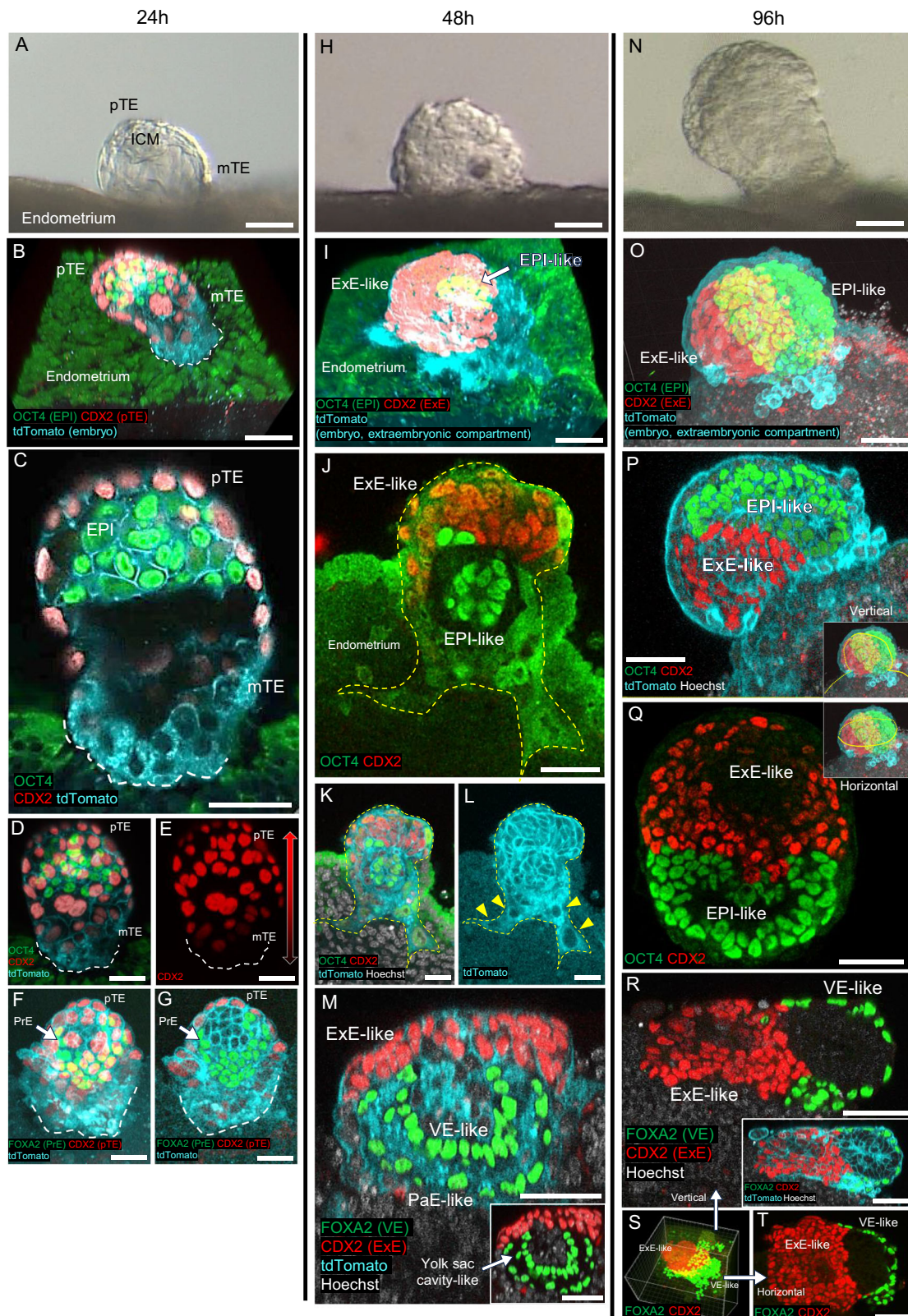


**Fig. 1 | Establishment of an ex vivo uterine system. A** Isolation of endometrial fragments from dpc 3.75 pregnant recipient mice and E3.75 blastocysts from donor mice. **B** A stereomicroscopic view of Isolated endometrium and endometrial fragments. Scale bar: 1 mm. **C** Specification of a PDMS ceiling. **D** A photograph of the co-culture of embryos and an endometrial fragment

on agarose gel covered with a PDMS ceiling. White arrow, an endometrial fragment. **E** Schematic illustration of ex vivo implantation system. **A**, **C**, and **E**. created with BioRender.com released under a Creative Commons Attribution-NonCommercial-NoDerivs 4.0 International license <https://creativecommons.org/licenses/by-nc-nd/4.0/deed.en>.





long-fixed condition, all embryos lost their embryonic morphology and appeared dead as integrated embryos at 72 h with a sparse number of cells (Supplementary Fig. 4B). Isolated embryos at 48 h showed flattened shapes, especially on their PDMS-facing side (Supplementary Fig. 4C), suggesting insufficient room for embryonic growth: On the other hand, embryos solely cultured on plastic and PDMS bottom dish presented a more advanced morphology at 96 h (Supplementary

Fig. 4D and E). This result was consistent with the previous long-term extended embryonic culture on a gas-permeable plate<sup>11</sup>, indicating that embryo development may tolerate a certain range of oxygen concentrations. These results suggest that the hampered embryonic development on the ex vivo uterus may not be attributable to the oxygen supply. Additionally, the advantages of sole culture over the PDMS-long-fixed co-culture were hypothesized as the following: a

**Fig. 2 | Embryogenesis on ex vivo uterus.** Time series observation of attached embryos at 24 h (A–G), 48 h (H–M), and 96 h (N–T). **A, H, N.** Stereoscopic findings. mTE attachment at 24 h (A), solid cell growth inside the blastocoel at 48 h (H), and embryonic expansion at 96 h (N) were observed on the endometria.  $n = 5$  (A), 4 (H), 7 (N) biologically independent samples. B–G, I–M, O–T. Whole-mount immunofluorescence. B–G. Confocal microscopic images at 24 h. A representative overhead view of a three-dimensionally reconstructed confocal image (B) was dissected in an oblique slice (C), and the front half of the embryo was depicted as overlays (D, E) to visualize CDX2 gradient from pTE to mTE (bilateral arrow). See also Movie S1. F, G. A representative 3D overhead view (F) and a slice (G) of attached embryos stained for CDX2 and a PrE marker FOXA2. White dotted lines indicate the attachment sites (D–G). I–M. Confocal microscopic images at 48 h. A representative 3D image (I) was dissected in an oblique slice (J, K, L), showing the emergence of EPI/ExE-like compartments (J, K) and nuclear enlargement of invading trophoblasts (arrowheads) (L). Yellow dotted lines indicate the surface of the embryo. See also Movie

S2. M. A representative slice from 3D image of whole-mount immunostaining for CDX2 and a VE marker FOXA2. FOXA2-positive undifferentiated PaE-like compartment and yolk sac-like morphology (inset) was identified. See also Movie S3. O–T. Confocal microscopic images at 96 h. A representative 3D image (O) was dissected in oblique slices (P, Q), showing a more organized form of EPI/ExE-like compartments than 48 h. See also Movie S4. R–T. Representative slices (R, T) from 3D image (S) of whole-mount immunostaining for CDX2 and FOXA2 show the presence of VE-like compartment. See also Movie S5. ICM, inner cell mass; mTE, mural trophoblast; pTE, polar trophoblast; PrE, primitive endoderm; EPI, epiblast; ExE, extraembryonic ectoderm; VE, visceral endoderm; PaE, parietal endoderm; Em, embryo. tdTomato indicates the cell membrane of all embryonic/extraembryonic cell lineages. Scale bars: 50  $\mu$ m. See also Supplementary Fig. 5 for the efficiencies and the number of independent experiments performed using different recipient animals.

spatial room for embryonic expansion, buoyancy to reduce embryonic self-weight to support their growth, and fresh and efficient nutrient supply from all directions in contrast to the stale and limited feeding from the one-way flow through the endometrium.

Considering these hypotheses, an optimized setting was finally discovered, in which a PDMS ceiling was removed at 24 h and the sample was immediately transferred to a neighboring shallow spot with 2 mm width, 3 mm length, and 1 mm depth (Fig. 1E). After PDMS removal, the central depth of the media in the spots settled down to ~300  $\mu$ m, probably resulting from the balance between the medium exudation and surface tension, conferring the developmental capacity of embryos and efficient nutrient and gas exchange. Under the setting, ~85% of embryos remained on the endometria at 48 h, developing in round shapes with solid cell growth in the blastocoel (Fig. 2H). Immunostaining for OCT4 and CDX2 identified epiblast (EPI)- and extraembryonic ectoderm (ExE)-like compartments (Fig. 2I–L, and Movie S2), suggesting the emergence of embryonic development corresponding to E5.25 embryonic stage. Immunostaining for FOXA2 found visceral endoderm (VE)-like, undifferentiated parietal endoderm (PaE)-like compartments, and yolk sac cavity-like space in between them (Fig. 2M, Movie S3). Extended culture to 96 h allowed further embryonic expansion with a more enlarged shape than 48 h (Fig. 2N). OCT4 and CDX2 immunostaining showed more advanced EPI and ExE-like structures with cavities in each compartment (Fig. 2O–Q, Movie S4), suggesting embryogenesis corresponding to E5.5 embryonic stage. FOXA2-positive VE-like structure was also found although yolk sac cavity-like and PaE-like morphologies were not detected (Fig. 2R, S, T, and Movie S5). Replicating embryogenesis on the ex vivo uterus above (Supplementary Fig. 5), we then set out to evaluate the authenticity of the system by single-cell RNA sequencing (scRNA-seq).

### scRNA-seq analysis validates bona fide implantation ex vivo

The scRNA-seq data of 24 h ex vivo embryos were aligned to the same clusters as in vivo embryos (Supplementary Fig. 6A), and exhibited appropriate lineage specification into *Pou5f1/Nanog/Sox2/Fgf4/Otx2/Klf4/Klf2*-positive EPI, *CDX2/Eomes/Elf5/Ddahl1/Gst1*-positive pTE, *Krt7/Krt8/Tfap2c/Irga7/Cald1/Hand1/Gata2*-positive mTE and *Gata4/Gata6/Foxa2/Pdfr/Cited1/Dab2/Gata6/Sox17/Sox7*-positive primitive endoderm (PrE), comparable to the E4.5 in vivo embryos (Supplementary Fig. 6B–E).

Next, the analysis of endometrial scRNA-seq also resulted in the same classification of ex vivo and in vivo endometrial cells including epithelial cells, stromal cells, vascular endothelial cells, and vascular smooth muscle cells (Fig. 3A–C, Supplementary Fig. 7A). Importantly, ex vivo uterus viably retained individual cell populations that can potentiate implantation, including glandular epithelial cells (Fig. 3B), *Bmp2/Wnt4/Klf5*-enriched decidual cells<sup>26</sup> (Fig. 3C, and Supplementary Fig. 7B) and immune cells such as innate lymphoid

cells (ILCs), B cells, and macrophages (Fig. 3A), which have never been included in the previous in vitro implantation models<sup>14,20–22,32</sup>.

Further, we performed interaction assay using embryonic and endometrial scRNA-seq data and detected numerous embryo-maternal crosstalk present ex vivo (Supplementary Fig. 8A–D) including interactions between embryonic cells and immune cells (Supplementary Fig. 8C and D). These findings again supported the fidelity of the ex vivo uterine system.

### Histology certifies authentic implantation and trophoblast invasion ex vivo

Next, we histologically validated ex vivo implantation sites. Whole-mount immunofluorescence revealed that the cultured ex vivo uterus retained three-dimensional (3D) architecture of FOXA2-positive glandular epithelium (GE) (Fig. 4A, Movie S6). The ex vivo uterus also preserved leukocytes including macrophages shown by the immunostaining of CD45 and F4/80 respectively (Fig. 4B, and Movie S7). KLF5-positive decidual cells<sup>26,33</sup> were found in the embryo-attached subluminal stroma (Fig. 4C). Vascular structures were also maintained, while notably the regions in the vicinity of attached embryos were avascular, which has been observed in in vivo studies and thought to be essential in preparation for the ensuing vascular remodeling<sup>34–36</sup> (Fig. 4D, Movie S8).

We then focused on the process of trophoblast invasion in the ex vivo uterus. It has been demonstrated that appropriate proliferation-differentiation-switching (PDS), with the cessation of proliferation in the uterine LE and the acceleration of proliferation in the stroma, is a well-established uterine receptivity marker and required for trophoblast intrusion following attachment<sup>9,37,38</sup>. The embryo-attached LE undergoes entosis and necroptosis<sup>27,28</sup> either necessitating non-proliferation status in the LE. Whole-mount Ki67 immunofluorescence visualized the preservation of receptive PDS with the negative staining in the LE and positive staining in the stroma in the cultured ex vivo uterus, prepared for trophoblast invasion (Fig. 4E, and Movie S9). Histological sections at 36 h revealed that CK8-positive trophoblasts started to break the epithelial barrier and intrude into the endometrial stroma (Fig. 4F), and at 48 h, invading trophoblasts eliminated uterine luminal epithelium (LE) as demonstrated by the immunostaining of E-cadherin (Fig. 4G) with present nuclear enlargement (Figs. 2L, 4G and 4H), indicative of the differentiation into the primary trophoblast giant cell (pTGC) lineage, which derives from mTE in the early phase of invasion<sup>39,40</sup>.

The ex vivo system, making it possible to sequentially replicate the aspects of embryonic attachment, trophoblast invasion, and embryogenesis (Supplementary Fig. 5), met the requirements for a faithful and reproducible implantation system. Notably, the fidelity and reproducibility were exceptionally high at 24 h, which led us to further dissect the authenticity of ex vivo implantation by further dissecting single-cell RNA sequencing (scRNA-seq).



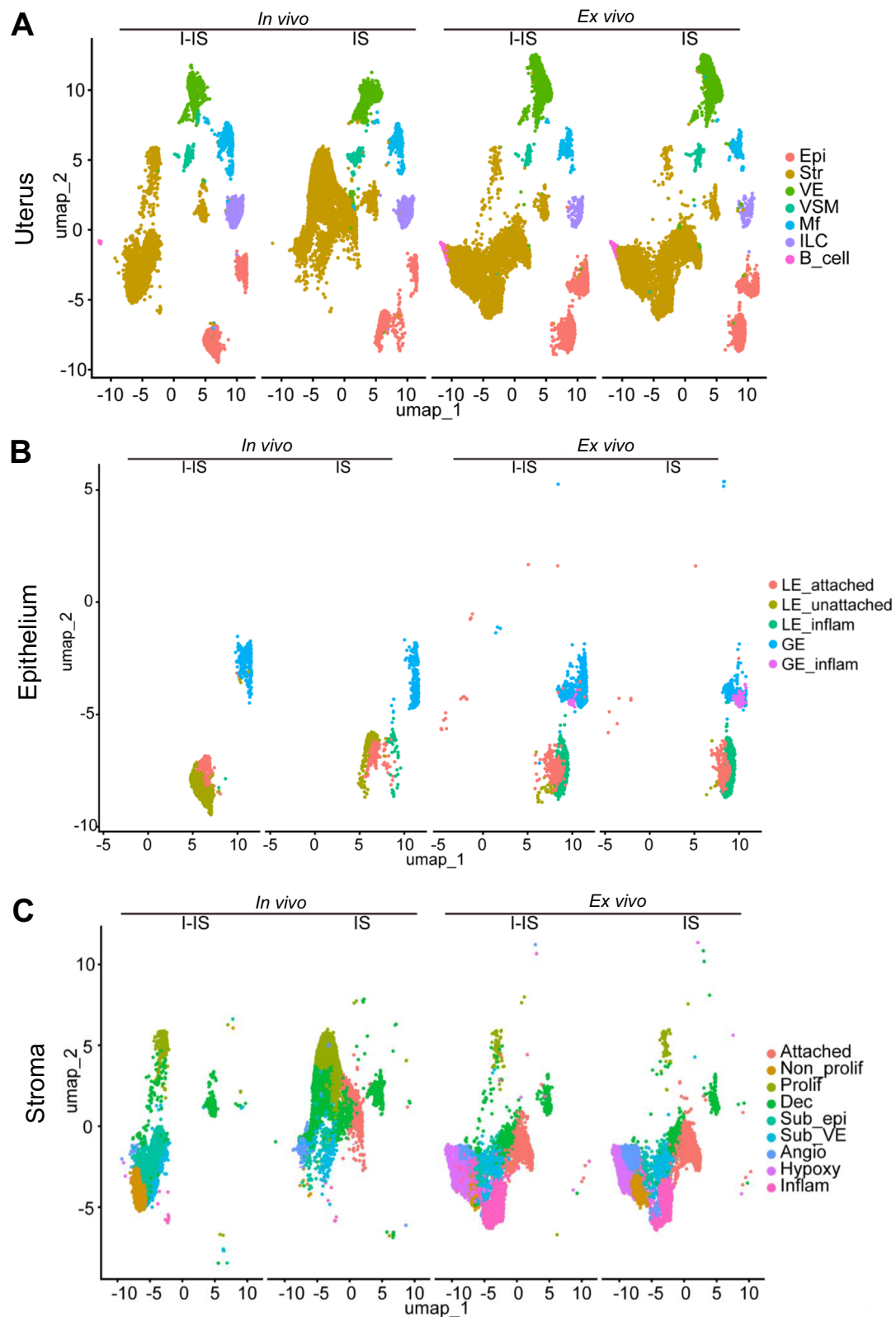
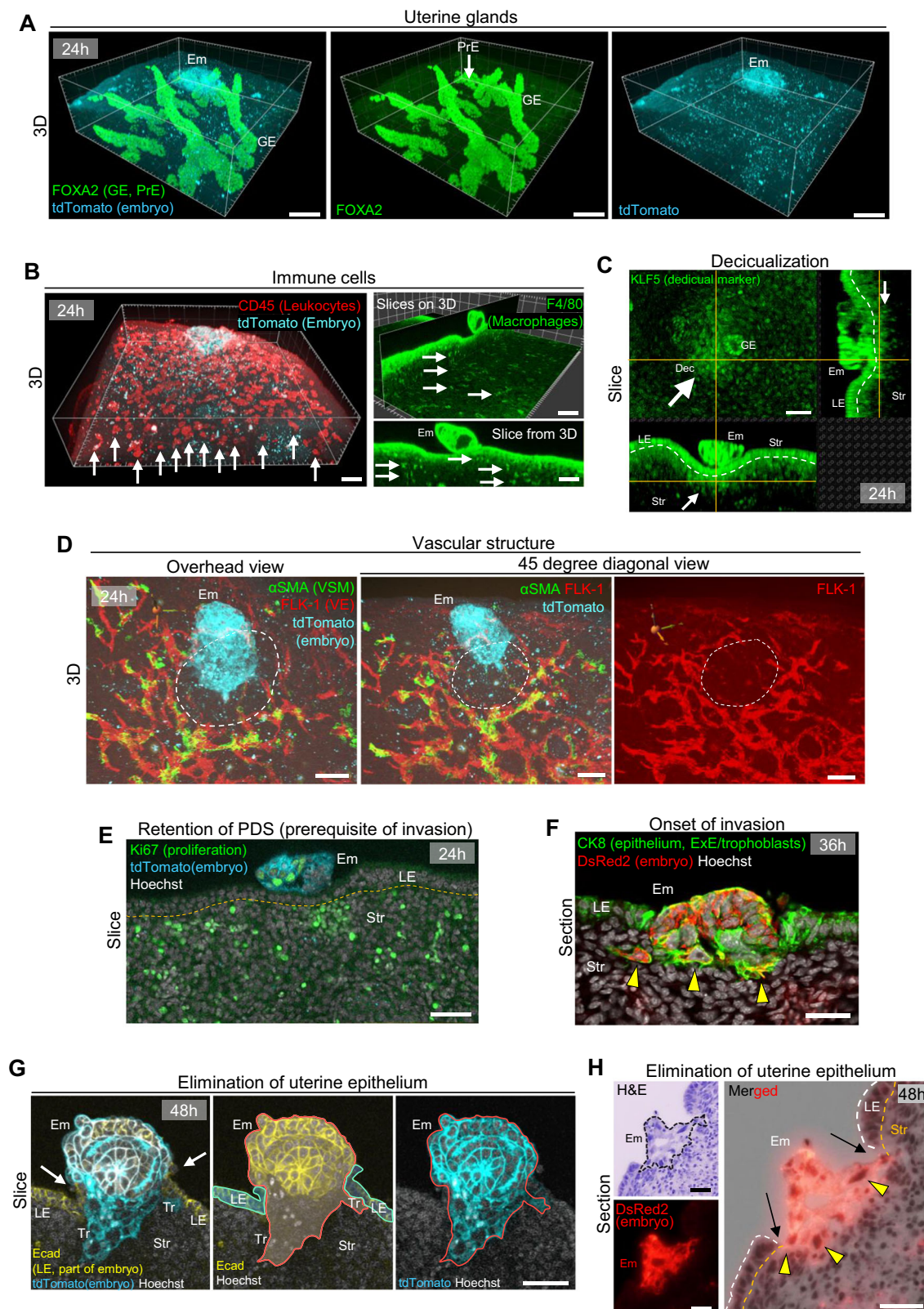


**Fig. 3 | Ex vivo uterus harbors genuine cellular components during culture.**

**A–C** The UMAP of single-cell RNA-seq of the whole endometria (**A**) showed similar cell clustering between in vivo and ex vivo. Epithelial cells and stromal cells were further profiled in **B**, **C**. Epi, epithelium; Str, stroma; VE, vascular endothelium; VSM, vascular smooth muscle; Mf, macrophages; ILC, innate lymphoid cells; LE\_attached, luminal epithelium at embryo-attached sites; LE\_unattached, luminal epithelium at embryo-unattached sites;

LE\_inflam, inflammatory luminal epithelium; GE, glandular epithelium; GE\_inflam, inflammatory glandular epithelium; Attached, the stroma of embryo- or PDMS-attached sites (attached stroma); Non\_prolif, non-proliferating stroma; Prolif, proliferating stroma; Dec, decidualized stroma; Sub\_epi, subepithelial stroma; Sub\_VE, subvascular endothelial stroma; Angio, pro-angiogenic fibroblasts; Hypoxy, hypoxic fibroblasts; Inflam, inflammatory fibroblasts.



### Robust induction of COX-2 in the ex vivo uterus

In vivo, cyclooxygenase-2 (COX-2), encoded by *Ptgs2*, is exclusively expressed at the attachment site of the endometrium. The role of COX-2 in the attachment reaction has been described previously, including studies with KO mice<sup>41</sup> and inhibitors<sup>42</sup>. Also, stromal COX-2 has been suggested to play an important role in decidualization<sup>26,41,43</sup>. Subclustering of stromal cells successfully identified *Ptgs2*-enriched

subluminal stromal clusters, named as attached stroma, both in vivo and ex vivo implantation sites (ISs) (Fig. 3C). While the cluster was not detected in in vivo inter-implantation sites (I-ISs), it was identified in ex vivo I-ISs (Fig. 3C). This may reflect an artificial inflammatory response to a non-self, PDMS. We then asked for gene ontologies (GOs) enriched in the attached stroma by Metascape. The analysis revealed the relevance to epithelial cell migration and blood vessel

**Fig. 4 | Ex vivo uterus retains uterine components with 3D architecture and captures the features of implantation.** **A** A representative 3D image of whole-mount immunofluorescence for FOXA2, a marker of uterine glands as well as embryonic PrE. See also Movie S6. **B** Representative 3D images of whole-mount immunofluorescence for CD45 and F4/80, markers of leukocytes and macrophages, respectively. White arrows indicate the presence of leukocytes and macrophages. See also Movie S7. **C** Slices from a representative 3D image of whole-mount immunofluorescence for a decidualization marker KLF5. White arrows indicate the induction of KLF5 in the embryo-attached subluminal stroma. Dotted line indicates the boundary between LE and stroma. **D** Representative 3D images of whole-mount immunofluorescence for FLK-1 and  $\alpha$ SMA, markers of VE and VSM, respectively. White dotted areas indicate the avascular region in the vicinity of the embryo attachment site corresponding to in vivo implantation. See also Movie S8. **E** A slice from representative 3D images of whole-mount immunofluorescence for a proliferation marker Ki67. The cultured ex vivo uterus sustains an appropriate

proliferation-differentiation switching (PDS) pattern, an index of uterine receptivity to the embryos. Note the cessation of proliferation in LE essential for ensuing trophoblast invasion. See also Movie S9. Dotted line indicates the boundary between LE and stroma. **F** Immunofluorescence of CK8 on histological sections at 36 h shows the onset of trophoblast invasion (arrowheads) into the stromal layer of the endometria. **G** A slice from a representative 3D image of whole-mount immunofluorescence for E-cadherin at 48 h shows the breach and elimination of uterine LE. tdTomato-negative uterine E-cadherin breaks at the boundary with the embryo indicated by white arrows. **H** H&E staining at 48 h exhibits enlarged nuclei in invading trophoblasts. White and orange dotted lines represent the surface of LE and the boundary between LE and stroma, respectively. PrE, primitive endoderm; Em, embryo; LE, luminal epithelium; GE, glandular epithelium; Str, stroma; Dec, decidua. DsRed2 or tdTomato indicates the mitochondria or cell membrane of all embryonic/extraembryonic cell lineages. Scale bars: 50  $\mu$ m. Three independent experiments with different recipient animals were performed for all the data.

morphogenesis (Fig. 5A and B), agreeing that embryo attachment is followed by decidual reactions accompanied by epithelial removal and angiogenesis<sup>27,28</sup>. Intriguingly, we found lipid biosynthetic process was enriched in the attached stroma (Fig. 5A and B). Recent studies have revealed that lipid metabolism pathways play roles in the fetomaternal interface<sup>43,44</sup>. Among the lipid-related pathways, prostaglandins (PGs) are crucial to the establishment of early pregnancy: uterine deletion of cyclooxygenases (COXs), rate-limiting enzymes for PG synthesis, results in embryo implantation failures<sup>43</sup>. Notably, *Ptgs2* (coding COX-2) was significantly highly expressed in the IS than I-IS of ex vivo attached stroma (Fig. 5C and D), underpinning its roles in implantation and also suggesting signals from embryos. Histological sections validated the localization of COX-2 in the vicinity of the embryo attachment sites in the ex vivo uterus at 24 h (Fig. 5E) and weak COX-2 induction in the subluminal stroma in ex vivo I-IS, presumably affected by PDMS (the right upper picture of Fig. 5E).

#### Ex vivo inhibition of uterine COX-2 reflects invasion defects reported in vivo

To verify the functional involvement of COX-2 in the ex vivo uterus, a selective COX-2 inhibitor celecoxib was administered. The results showed a decrease in the attachment rate at 24 h and a significant increase in the shedding rate of attached embryos between 24 h and 48 h, with only about a quarter of the embryos finally remaining at 48 h. (Fig. 5F–I). Importantly, three-dimensional confocal images with a clearing reagent enabled concise and vivid observation of trophoblast invasion in the ex vivo uterus and its quantification, which has been challenging in in vivo studies. As a result, even remaining embryos at 48 h showed significantly fewer invasion volumes in the ex vivo uterus (Fig. 5J and K). These findings mirrored the defective trophoblast invasion reported in a study using a celecoxib administration model<sup>42</sup> and systemic or uterine-specific COX-2 KO mice<sup>41,43</sup>. Importantly, the present findings would result from the effect of celecoxib primarily on the endometria, rather than the embryos, because the expression level of COX-2 in the embryo was low (Fig. 5E) and systemic COX-2 deficiency did not lead to embryonic lethality<sup>45</sup>.

#### FBS exhibits insufficient COX-2 induction and defective trophoblast invasion

In establishing the system, we discovered apparent inferiority in FBS to KSR. Previous studies on embryonic long-term sole culture utilized the IVC1 medium based on 20% FCS with heat inactivation (HI) for the first part of the culture (~48 h<sup>11,21</sup>) and it was replaced with the IVC2 medium based on 30% KSR<sup>11,21</sup>. With 20% FBS with or without HI, our system exhibited a significantly lower number of embryonic sustenance at 48 h than that with the EXiM medium, with a decreasing trend of attachment efficiency at 24 h (Supplementary Fig. 9A and B). HI process in FBS slightly retarded the outcomes without significant statistical

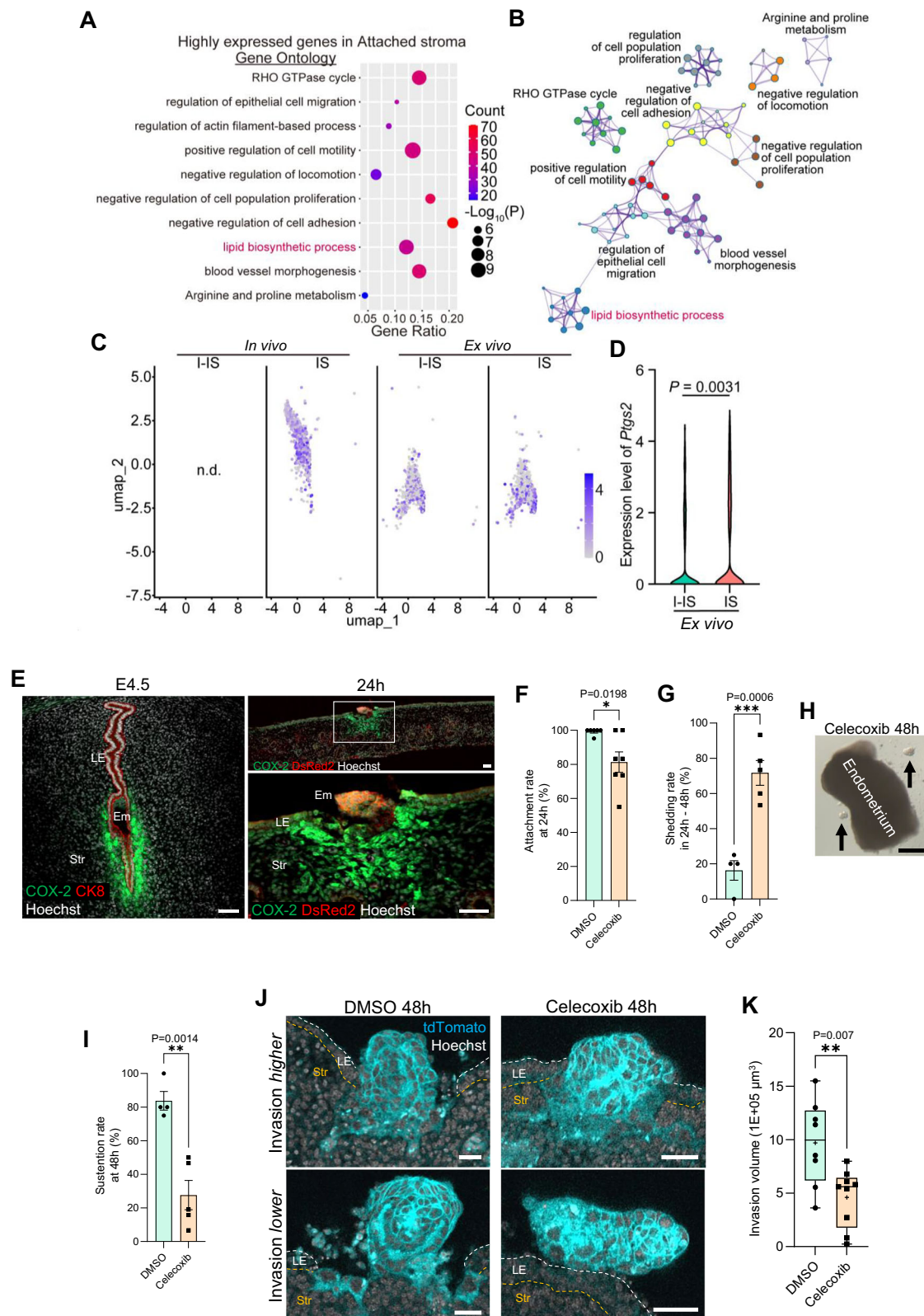
differences (Supplementary Fig. 9A and B), and FBS with a different lot reproduced the above findings (Supplementary Fig. 9C and D). The increment of FBS up to 30% presented worse results (Supplementary Fig. 9A and B), indicating a negative effect of FBS itself on implantation. When solely cultured, however, embryos adhered and expanded on the plastic and PDMS bottom dish with FBS, compatible with the previous report<sup>11</sup>. On the contrary, the EXiM medium did not induce attachment to the dish (Supplementary Fig. 9E). These findings suggested that the effect of FBS and KSR highly depends on embryonic attachment counterparts.

In reflection on the advantage of KSR over FBS in the ex vivo system, we focused on the previous reports that attributed the strength of KSR in tissue culture to a lipid-rich ingredient AlbuMAX<sup>23</sup>, which brought us to suspect the functional involvement of lipid-associated cascade in the ex vivo system. Accordingly, immunofluorescence of COX-2 revealed a significant reduction at attachment sites at 24 h with 20% FBS without HI (Supplementary Fig. 9F and G), suggesting that the cause of the inferiority of FBS might be attributable, at least in part, to its inability to induce endometrial COX-2.

#### Maternal COX-2 affects embryonic AKT

We next returned to the original protocol using KSR and sought to clarify the downstream mechanism of uterine COX-2. First, the bulk RNA-seq analysis of ex vivo embryos revealed that celecoxib treatment dramatically increased differentially expressed genes (DEGs) in the embryos attached to the uteri rather than solely cultured ones, suggesting celecoxib affects embryos by changing the endometrial conditions (Fig. 6A, Supplementary Table 1A). In addition, treatment with celecoxib did not significantly affect the developmental efficiency under sole-culture conditions on PDMS bottom dishes (Supplementary Fig. 10A and B), which is consistent with the previous report on COX-2 KO embryos<sup>45</sup> and also suggested negligible off-target effects of celecoxib on embryos other than COX-2 pathways. The pathway enrichment analysis found celecoxib downregulated AKT pathways in the ex vivo embryos cultured with endometria (Fig. 6B, Supplementary Table 1B). It has been reported that uterine deletion of hypoxia-inducible factor 2a (HIF2A) elicited defective trophoblast invasion with decreased AKT phosphorylation<sup>46</sup>. AKT, including family proteins AKT1, AKT2, and AKT3, is involved in cell survival, migration, invasion<sup>47</sup>, and even placentation. AKT1 KO neonates are small with increased neonatal mortality and show placental hypotrophy<sup>48–50</sup>. AKT1/AKT3 double KO mice exhibited embryonic lethality due to defective placental formation<sup>51</sup>. Because several stimuli can promote AKT phosphorylation including integrins, cytokines, growth factors, and even lipid mediators<sup>47</sup>, we suspected that the endometrial COX-2 may affect embryonic AKT and regulate trophoblast invasion. The histological sections on dpc 5.5 (E5.5) identified AKT expression and its phosphorylation in the invading trophoblasts in the vehicle group,





consistent with the previous study<sup>46</sup>. However, AKT activation was downregulated in the invading trophoblasts by maternal celecoxib treatment (Fig. 6C and D) as well as uterine COX-2 deletion<sup>43</sup> (Supplementary Fig. 11). Likewise, immunofluorescence of phospho-AKT (pAKT) on 48 h ex vivo revealed that AKT was activated in the CK8-positive/CDX2-negative invading trophoblasts (Supplementary Fig. 12), and was significantly deactivated by celecoxib administration

(Fig. 6E–H), suggesting a possible interaction between uterine COX-2 and embryonic AKT. This conjecture was supported by the results of GSEA pathway analysis that the ISs of the ex vivo uteri exhibited significant reduction in “Activation of AKT signaling” by celecoxib (Supplementary Table 2) as well as the downregulation of prostaglandin metabolic process (Supplementary Table 2, Supplementary Fig. 13 derived from downregulated DEGs list shown in Supplementary

**Fig. 5 | Ex vivo uterus replicates robust induction of COX-2 and mirrors decreased trophoblast invasion by COX-2 inhibition.** **A, B** Gene ontology analysis of uterine scRNA-seq found enriched lipid metabolic pathways in the attached stroma clustered in Fig. 3C. Modified Fisher's exact test with P value cutoff 0.05 was used (**A**). **C** Attached stroma was detected in in vivo implantation site (IS) and ex vivo inter-implantation site (I-IS) and IS. **D** *Ptgs2* expression in ex vivo attached stroma was highly induced in IS (attached by embryo) compared to I-IS (attached by PDMS), suggesting robust signals from embryos. The *P*-value was calculated by two-tailed Mann-Whitney's U-test. **E** Immunofluorescence of COX-2 on histological sections detects localized expression of COX-2 exclusively at the attachment sites of the endometria both in vivo and ex vivo. **F–K** A COX-2 inhibitor celecoxib retards embryonic attachment and trophoblast invasion. Each graph represents the percentage of embryos that attached at 24 h/initially loaded (**F**), shed between 24 h and 48 h/attached at 24 h (**G, H**), and sustained on the endometria at 48 h/initially

loaded (**I**). Mean  $\pm$  SEM (**F, G, I**). A stereomicroscopic photo (**H**) shows spontaneously shed embryos at 48 h indicated by arrows. Scale bar: 500  $\mu$ m. Slices from three-dimensional images show representative trophoblast invasion (**J**). Examples of higher and lower invasions in each group were presented and the invasion volume was compared (**K**). The box plot is presented as minimum, lower quartile, median, upper quartile, and maximum. + represents the mean value. White and orange dotted lines represent the surface of LE and the boundary of LE and Str, respectively. Two-tailed unpaired Student's *t*-test (**F, G, I, K**) was used ( $n = 6$  vs  $7$  (**F**),  $4$  vs  $5$  (**G**),  $4$  vs  $5$  (**I**),  $8$  vs  $9$  (**K**) biologically independent samples). \*,  $P < 0.05$ ; \*\*,  $P < 0.01$ ; \*\*\*,  $P < 0.001$ . White and orange dotted lines represent the surface of LE and the boundary of LE and Str, respectively. DsRed2 or tdTomato indicates the mitochondria or cell membrane of all embryonic/extraembryonic cell lineages. Scale bars: 50  $\mu$ m. Each plot represents the result per a recipient mouse (**F, G, I**) or the value for an embryo (**K**).

Table 3). The data also found a significant decrease in EGF/VEGF/NGF/ERBB2 signaling and insulin signaling that can activate AKT pathway<sup>47</sup> (Supplementary Table 2).

### Suppression of embryonic AKT induces decreased trophoblast invasion

To validate the role of AKT in trophoblast invasion ex vivo, a pan-AKT inhibitor MK-2206 2HCl was administered. As a result, although embryonic attachment at 24 h did not significantly change at both 10  $\mu$ M and 100  $\mu$ M (Fig. 6I), all attached embryos shed off at 48 h at 100  $\mu$ M (Fig. 6J and K). In addition, the remaining embryos at 48 h at 10  $\mu$ M showed a significant decrease in invasion volume (Fig. 6L and M). The above findings agreed with the previous in vivo studies showing defective placentation in AKT(s) KO embryos.

### Embryonic AKT1 transduction ameliorates celecoxib-induced defective implantation both ex vivo and in vivo

Next, we examined whether the celecoxib-induced implantation defects could be recovered by the embryonic treatment with adeno-associated virus type 1 (AAV1) carrying N-terminally myristoylation signal-attached AKT1 (myr-AKT1), a constitutively active form of mutant AKT1<sup>52</sup>. In vitro fertilization (IVF)-derived embryos at their blastocyst stage were pretreated with myr-AKT1-carrying AAV1 (myr-AKT1-AAV1) for 6 h (Fig. 7A). Higher immunoreactivities of pAKT in solely cultured embryos with myr-AKT1-AAV1 treatment than non-treatment indicated successful AKT1 introduction and its activation, which started from 24 h and remained positive at 48 h (Supplementary Fig. 14A and B). Then, the pretreated embryos were assessed for implantation capacity ex vivo. As a result, significantly more embryos remained on the endometria at 48 h with myr-AKT1-AAV1 pretreatment than that with EGFP-AAV1 treatment in the presence of celecoxib (Fig. 7B and C). Also, the invasion volume was significantly improved by myr-AKT1-AAV1 treatment (Fig. 7D and E), suggesting a possible signaling that links uterine COX-2 and embryonic AKT1. The inability to recover the sustention rate at 48 h to the extent of DMSO + EGFP-AAV1 group (Fig. 7C) could be linked to the decreased adhesive capacity by celecoxib both in the embryos (Fig. 6B) and the ISs of the uteri (Supplementary Fig. 13, Supplementary Table 2). Embryonic myr-AKT1-AAV1 treatment also showed a trend for amelioration of invasion volume under a setting of 20% FBS w/o HI albeit without a statistical significance ( $P = 0.0906$ ) (Supplementary Fig. 9H–K), suggesting a partial efficacy of AKT1 transduction to alleviate the defects by COX-2 insufficiency and also its limitation to recover other unknown defects with FBS.

Finally, we validated whether the above findings applied to in vivo conditions. With a previously established protocol of celecoxib administration to induce defective trophoblast invasion and decidualization<sup>42</sup>, we aimed to improve the celecoxib-induced implantation defects with myr-AKT1-AAV1 embryonic treatment

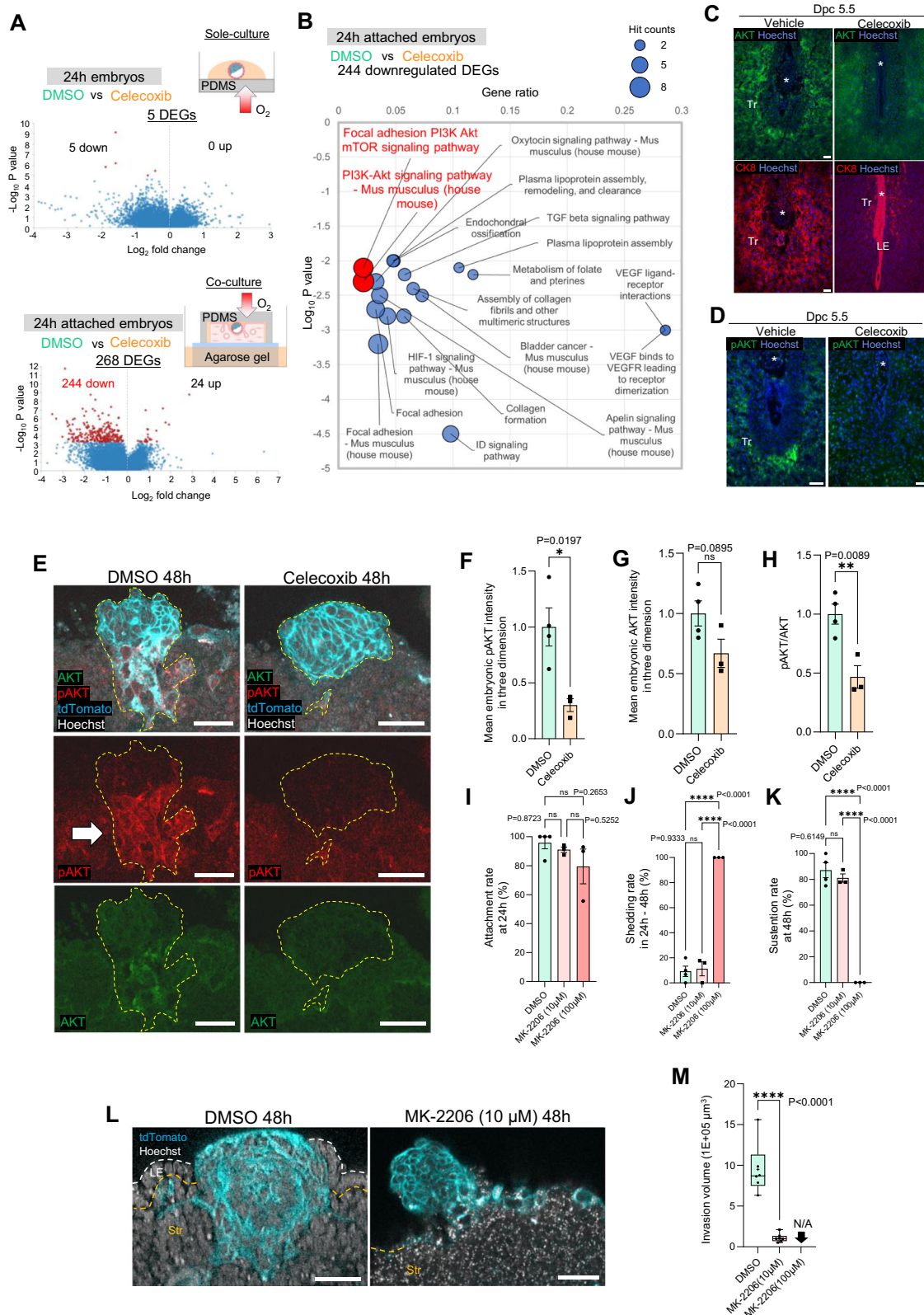
before blastocyst transfer (Fig. 7F). As a result, myr-AKT1-AAV1 significantly ameliorated the reductions in the weight of IS and trophoblast invasion (Fig. 7G–J), proposing a putative link of uterine COX-2/embryonic AKT1 present in vivo (Fig. 7K). These findings reinforced not only the fidelity of the system but also the potential to unveil unknown biology and develop therapies for recurrent implantation failure.

## Discussion

In this study, we successfully established an ex vivo uterine system that replicated the whole implantation process encompassing embryonic attachment, trophoblast infiltration, and embryogenesis on the uterus as an integrated organ. Our system retained essential uterine components and highly captured features in implantation, including decidual cells, immune cells, glandular epithelium, vascular structure with appropriate patterning, and sustentation of proper PDS, which were missing in previous models<sup>14,20–22,32</sup>. Significantly, the present system induced maternal COX-2 in the vicinity of the attached embryo, a critical maternal implantation regulator, without overexpression. The system, recapitulating authentic embryo implantation in terms of maternal-embryonic signaling, enables reproducible and concise screening of implantation and shows superiority to in vivo studies in that the experimental condition can be modulated in the same animal. Also, the system offers the potential to investigate the roles of immune cells and their functional interaction with the uterus and embryos ex vivo with the preservation of the original uterine cell component, since it has been reported that immune cells can affect embryo implantation in vivo<sup>33,54</sup>.

While in vitro embryogenesis models using authentic embryos, blastoids, and synthetic embryos hold great promise, they have yet to achieve viable offspring even in mice, potentially highlighting the critical role of embryo-uterine interactions during development. Our system addresses this limitation by involving uterine components, offering a unique opportunity to extend ex vivo embryogenesis through the interaction in the future. Further improvements to our system may enable a longer-term ex vivo embryonic culture while maintaining physiological relevance, as stem cell-based models have advanced over time through optimizations<sup>16,17</sup>.

In developing the system, the use of KSR, not FBS, was one of the most decisive factors. The reason why KSR was better than FBS may be attributable to its benefits in tissue culture. Since the composition of KSR is undisclosed, determining the responsible elements in KSR is challenging. However, a study has discovered that it was AlbuMAX, a lipid-rich BSA, that contributed to the effectiveness of KSR in tissue culture<sup>23</sup>. Moreover, they further narrowed down the responsible elements and identified a lipid mediator lysophosphatidic acid (LPA) and its precursors as especially effective ingredients in AlbuMAX<sup>55</sup>. Because previous studies have revealed that LPA evokes embryo implantation and decidual reactions by up-regulating COX-2<sup>37,56</sup>, and LPC, a



precursor of LPA, was considerably highly contained in AlbuMAX<sup>55</sup>, it was reasonable that the lipid cocktail carried in AlbuMAX in KSR supported ex vivo implantation. The slightly worse results with HI of FBS may imply that FBS also contains any beneficial ingredients for implantation, such as cytokines or growth factors, incapacitated by HI. From the viewpoint of embryonic culture, a previous study highly recommended using high-quality embryonic stem cell-grade FCS and

individual testing of each batch to assess the culture efficiency<sup>11</sup>. Therefore, using a desirable batch of FBS could have enabled successful co-culture in the present system. Nevertheless, in terms of the advantages of tissue culture efficiency, time-sparing without screening, and high reproducibility, we would recommend the use of KSR for the current system. Further mechanistic explorations on the medium composition including AlbuMAX and its dosage are necessary to



**Fig. 6 | Ex vivo uterine system suggests a possible signaling that mediates uterine COX-2 and embryonic AKT.** **A** Bulk RNA-seq of embryos cultured solely and co-cultured with ex vivo uterus for 24 h. The number of DEGs increased in the co-cultured embryos attached to the endometria, suggesting the effect of celecoxib predominantly on the uterus and the signals from the uterus to embryos. DESeq2 Wald test with an adjusted P value cutoff 0.05 using the Benjamini and Hochberg method for multiple testing was performed. The plots were automatically generated by RaNA-seq, and the vertical axis shows the P value before adjustment. **B** A bobble plot of enrichment analysis on the 244 downregulated DEGs (**A**) by celecoxib exhibits the suppression of embryonic AKT signaling in ex vivo co-cultured embryos. See also Supplementary Table 1A and B. Accumulative hypergeometric test was used, and all the results involving KEGG Pathway, Reactome Gene Sets, and WikiPathways showing  $\log_{10} P$  value less than -2 were plotted. **C** Representative pictures of immunofluorescence for AKT and CK8 in sequential sections. **D** Representative pictures of immunofluorescence for pAKT. Asterisks indicate the location of embryos and three independent experiments with different animals were performed (**C**, **D**). **E** Representative slices from three-dimensional images of whole-mount immunofluorescence for AKT and pAKT with celecoxib treatment. Yellow dotted lines indicate the outline of the embryos. The white arrow

indicates the activation of AKT in invading trophoblasts. Three-dimensional mean fluorescent intensity values within the surface were computed by Imaris. Each value for AKT (**F**), pAKT (**G**), and pAKT/AKT (**H**) in DMSO group were normalized to 1. Mean  $\pm$  SEM. **I** Attachment at 24 h/initially loaded. **J**. Shedding between 24 h and 48 h/attached at 24 h. **K**. Sustention on the endometria at 48 h/initially loaded. Mean  $\pm$  SEM (**I–K**). **L** Representative slices from three-dimensional images. **M**. Quantitative data of the invading volumes. The box plot is presented as minimum, lower quartile, median, upper quartile, and maximum. + represents the mean value. LE, luminal epithelium; Str, stroma. Two-tailed unpaired Student's t-test (**F**, **G**, **H**, **M**) and ordinary one-way ANOVA with post hoc Tukey's multiple comparisons test (**I**, **J**, **K**) were used ( $n = 4$  vs 3 (**F–H**), 4 vs 3 vs 3 (**I–K**), 6 vs 7 (**M**) biologically independent samples). \*,  $P < 0.05$ ; \*\*,  $P < 0.01$ ; \*\*\*\*,  $P < 0.0001$ ; ns, not significant. tdTomato indicates the cell membrane of all embryonic/extraembryonic cell lineages. White and orange dotted lines represent the surface of LE and the boundary of LE and Str, respectively. Scale bars: 50  $\mu$ m. Each plot represents the result per a recipient mouse (**I–K**) or the value for an embryo (**F–H**, **M**). Scale bars: 50  $\mu$ m. A. created with BioRender.com released under a Creative Commons Attribution-NonCommercial-NoDerivs 4.0 International license (<https://creativecommons.org/licenses/by-nc-nd/4.0/deed.en>).

identify the genuinely bioactive compounds and to develop further efficient conditions.

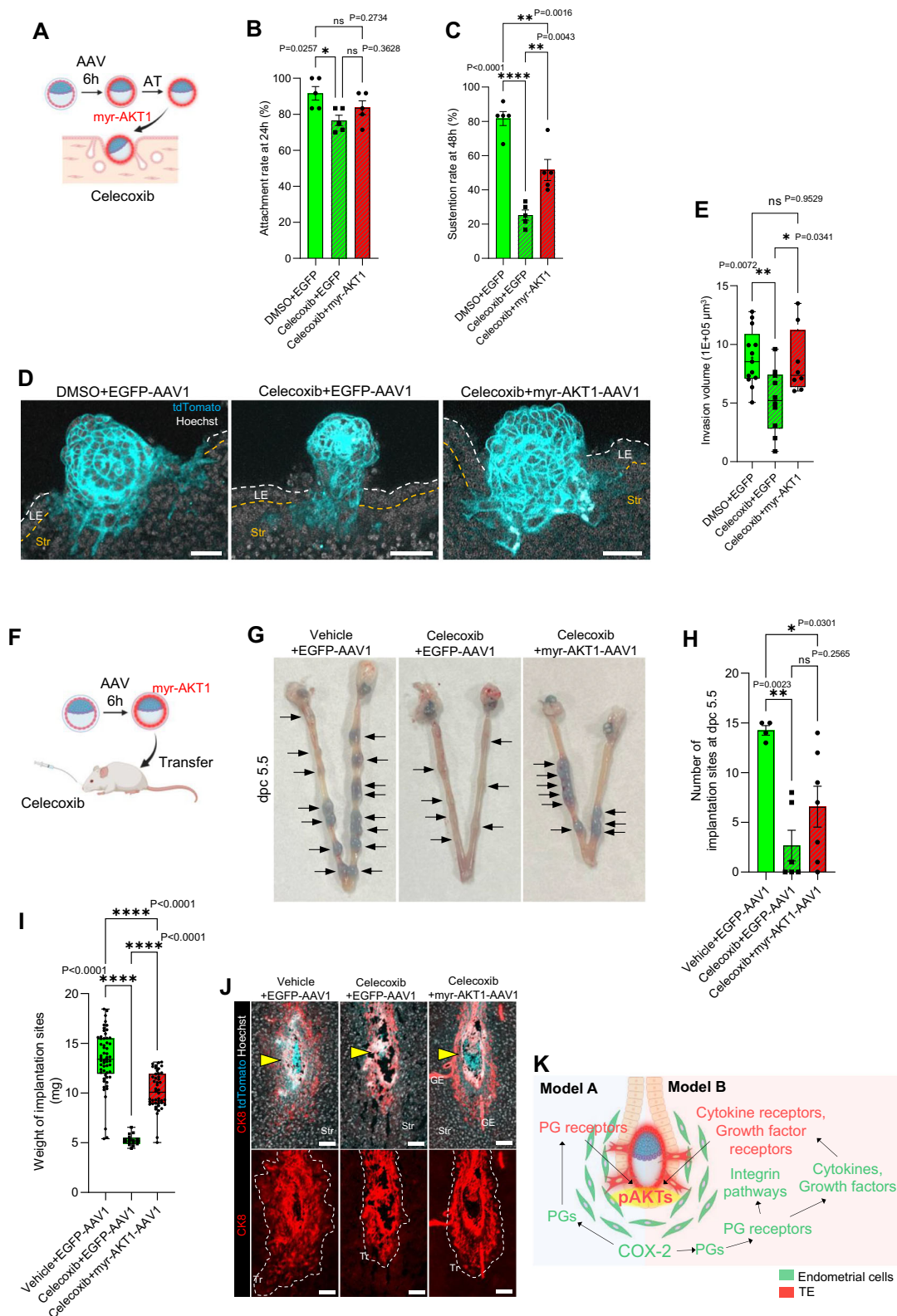
Optimization of the ovarian hormone levels was also a critical determinant. As already established in previous studies, excessive estrogen badly affects embryo implantation<sup>26,38,57</sup>. An imbalance in estrogen and progesterone levels causes aberrant expression of key implantation regulators, and results in an inappropriate condition of proliferation-differentiation switching (PDS) in the epithelium and stroma, presenting impaired endometrial receptivity<sup>38,57,58</sup>. The defective ex vivo implantation on the PMSG-stimulated endometria will reflect human ART cases, where fresh embryo transfer is not preferred immediately after high ovarian stimulation to circumvent the harmful effects of high estrogen. Because the estrogen levels in the IVC1 and IVC2 medium<sup>11</sup> were much higher (8 nM) than the physiological level<sup>8,25</sup>, optimizing ovarian hormone levels was necessary. The similar results between 3 pg/mL and 30 pg/mL may probably derive from the range of the physiological estrogen level from 3 to 30 pg/mL according to different reports<sup>8,25</sup>. Nevertheless, we recommend 3 pg/mL estrogen level because of the slightly better results compared to 30 pg/mL (Supplementary Fig. 1D).

Another fundamental point was the oxygen supply. Initially, we had estimated that the oxygen supply from the stromal end through the PDMS bottom would be reasonable because, in physiological settings, oxygen is thought to be delivered via stromal blood vessels. However, the results turned out to be the opposite. Since there has been no reliable data on the oxygen concentration in the uterine lumen, providing a reasonable explanation for the result is difficult. However, a possible mechanism is that the uterine lumen is not as hypoxic as presumed because the uterine lumen is connected to the outside of the body under 21% oxygen through the vagina, similar to the digestive tract. Indeed, a previous study reported that the embryos did not show hypoxia even though the surrounding endometria were hypoxic<sup>59</sup>. The trials with regard to the efficiency of oxygen supply suggest the presence of a threshold of oxygen levels in enabling implantation (Supplementary Fig. 1A and B). Because it was technically difficult to settle embryos on the endometria in the gel spots with shallow media over the endometria (24–96 h condition in Fig. 1E) and the results in PDMS-free and 50  $\mu$ m-thick PDMS ceiling condition were worse, the present system necessitates PDMS device with a certain thickness, although the exact oxygen concentration in the tissue facing PDMS in comparison with that in physiological conditions is unknown without specific reports. Modulation of oxygen concentration in an incubator may provide further mechanistic insights and resolution for a potential drawback in PDMS with artificial effects and an obstruction

for reproduction by other researchers unless it is commercially available. Nevertheless, it could be plausible that embryo development might have the flexibility to tolerate a wider range of oxygen concentrations (Supplementary Fig. 4D and E) compared to the phenomenon of implantation.

Compatible with in vivo embryo implantation, our study did not identify pTE attachment to the endometria, implicating higher adhesiveness of mTE than pTE. In this regard, the few detached embryos at 24 h might have had the pTE side primarily facing the endometrium at initial placement. On the other hand, the location of embryos in the present system was not as relevant as in the physiological settings, where embryos are evenly distributed and implant at the bottom of the crypt<sup>26</sup>. These phenomena, so-called spacing, seemed not critical in the ex vivo system because the alignments did not produce any significant difference in implantation efficiency, with embryos randomly placed, robustly attaching, and intruding. Because the mechanism of spacing has not been fully elucidated yet, our findings might propose that the attachment reactions can be triggered at the site of embryos, apart from the mechanism of spacing, which might be regulated by myometrial contraction or endometrial peristalsis.

The localized induction of COX-2 at attachment sites was highly reproducible in the present system. Although it has been established that uterine COX-2 is crucial for embryo implantation and decidualization through PGE2 and PGD2 production<sup>43</sup>, the specific downstream mechanism remained elusive. According to a previous study<sup>46</sup>, we focused on AKT. Among the AKT isoforms, AKT1 shows the most common and significant association with cancer progression and treatment response across various cancer types, making it a critical target for cancer therapy<sup>60</sup>. The mechanism of how endometrial COX-2 regulates embryonic AKT can be explained by two distinct models depending on whether endometrial PGs directly or indirectly affect the embryos (Fig. 5K). Because PG receptors-KO mice can be viably produced<sup>61–65</sup>, it might be reasonable to hypothesize that endometrial PGs do not directly impact embryos but rather the endometrium. PGs promote expressions of cytokines and growth factors that may promote embryonic viability and trophoblast invasion through paracrine mechanisms. It is also possible that COX-2-mediated integrin activation, as suggested in angiogenesis and cancer metastasis<sup>66,67</sup>, may participate in AKT activation. Indeed, our results of bulk RNA-seq of embryos and uteri suggested the insufficient attachment at the embryo-maternal interface (Fig. 6B, and Supplementary Fig. 13, Supplementary Table 2) as well as the suppression of EGF/VEGF/NGF/ERBB2 signaling and insulin signaling in the uteri (Supplementary Table 2), which potentially activate AKT pathway<sup>47</sup>. Based on the



present screening, future studies should address the more specific molecular mechanisms that link uterine COX-2 and embryonic AKT by utilizing genetic models.

Transfection of a constitutively active form of AKT1 with AAV1 significantly ameliorated celecoxib-induced trophoblast invasion defects. AAVs are small non-enveloped viruses, gathering attention as vectors for gene therapy in several organs<sup>68,69</sup>. AAVs can offer several

advantages, such as high transfection efficiency and capacity in both dividing and non-dividing cells, long-term gene expression, and permeability for the zona pellucida of the embryos<sup>70,71</sup>. Unlike lentiviruses (LVs), which do not show zona permeability, the effects of AAVs are temporal, making it possible to avoid disadvantages caused by genomic integration and permanent overexpression, such as oncogenesis. The embryonic activation of AKT did not cause the complete rescue of

**Fig. 7 | Embryonic AKT1 transduction ameliorates invasion defects in the uteri with celecoxib administration ex vivo and in vivo.** **A–E** Ex vivo experiments. **A** schematic diagram of the ex vivo rescue for celecoxib-induced invasion defect using myr-AKT1-AAV1. **AT**, acidified Tyrode's solution. **B** Attachment at 24 h/initially loaded. **C**, Sustention on the endometria at 48 h/initially loaded. Mean  $\pm$  SEM (**B**, **C**). **D** Representative slices from three-dimensional images. **E**, Quantitative data of the invading volume. The box plot is presented as minimum, lower quartile, median, upper quartile, and maximum. + represents the mean value. **F–J** In vivo experiments. **F** A schematic diagram of the in vivo rescue for celecoxib-induced implantation defect using myr-AKT1-AAV1. **G** The uteri at dpc 5.5 after intravenous injection of blue dye solution. Implantation sites (ISs) are indicated by arrows. **H** Number of IS per mouse. 16 embryos were transferred to each pseudopregnant mice. Mean  $\pm$  SEM. **I** The weight of IS. The box plot is presented as minimum, lower quartile, median, upper quartile, and maximum. + represents the mean value. **J** Representative photos of immunofluorescence for CK8 on histological sections. Trophoblast invasion was limited in celecoxib+EGFP-AAV1 group compared to

vehicle+EGFP-AAV1 and celecoxib+myr-AKT1-AAV1 groups. Yellow arrowheads represent embryos. White dotted line indicates the outer border of invading trophoblasts. GE, glandular epithelium; Str, stroma; Tr, trophoblast. Ordinary one-way ANOVA with post hoc Tukey's multiple comparisons test (**B**, **C**, **E**, **H**, **I**) was used ( $n = 5$  vs  $5$  vs  $5$  (**B**, **C**),  $13$  vs  $10$  vs  $8$  (**E**),  $4$  vs  $6$  vs  $7$  (**H**),  $57$  vs  $16$  vs  $46$  (**I**) biologically independent samples). \*,  $P < 0.05$ ; \*\*,  $P < 0.01$ ; \*\*\*\*,  $P < 0.0001$ ; ns, not significant. tdTomato indicates the cell membrane of all embryonic/extraembryonic cell lineages. Scale bars:  $50\ \mu\text{m}$ . **K** Proposed models of how uterine COX-2 activates embryonic AKT. In model A, PGs bind to PG receptors in TE and activate AKT. In model B, cytokines and growth factors produced downstream of endometrial PG receptors accelerate AKT phosphorylation. Each plot represents the result per a recipient mouse (**B**, **C**, **H**) or the value for an embryo (**E**, **I**). **A**, **F**, and **K** created with BioRender.com released under a Creative Commons Attribution-NonCommercial-NoDerivs 4.0 International license (<https://creativecommons.org/licenses/by-nc-nd/4.0/deed.en>).

embryo implantation impaired by celecoxib, which could be due to the alteration of many other pathways in the embryos other than AKT (Fig. 6B). The simultaneous transfection of myr-AKT2 and myr-AKT3 may produce better results or may not because there must be other molecules responsible for trophoblast migration such as RAC1<sup>21</sup>. For another, endometrial ECM remodeling by MMPs will also be involved in trophoblast invasion<sup>46</sup>. FBS caused more severe invasion retardation than that induced by celecoxib administration (Fig. 5K and Supplementary Fig. 9K), suggesting the presence of undetermined defects in addition to COX-2 insufficiencies (Fig. 6B).

In its present form, the ex vivo system has several limitations. For example, embryos did not grow beyond the E5.5 stage even after 96 h in the present study. Likewise, the reproducibility of EPI-associated development was not high compared to trophoblasts/ExE-associated hallmarks (Supplementary Fig. 5). The yolk sac cavity-like structure at 48 h was not present at 96 h, presumably associated with the unsuccessful differentiation of PrE into FOXA2-negative PaE at 48 h (Fig. 2M). One possible reason was that culturing preimplantation blastocysts long-term is challenging compared to postimplantation blastocysts as suggested in previous studies<sup>11,12</sup>. Secondly, whether the present condition is ultimately suited for endometrial tissue culture is still inconclusive. Also, the EXiM medium, specialized for embryonic attachment and invasion, may not be as favorable for embryonic development as the sequential use of the IVC1 and IVC2 medium. Moreover, the present model is structurally planar, different from the physiological mouse uterine geometry in which embryos are encapsulated in cylindrical LE, attached at the bottom of the crypt, and then naturally enclosed deep inside the endometria just by the elimination of LE barriers. Further exploration for even better conditions is necessary to facilitate further embryonic growth, including an exploration of basal media, nutrients, additives, oxygen concentration, and biomaterials. An apparatus that enables an efficient medium supply and gas exchange without disturbing the room for embryonic expansion might facilitate further embryogenesis on the endometria. Also, given that long-term culture of seminiferous tubules has been successfully maintained for two months<sup>23</sup>, it would be of importance to investigate the potential duration for which long-term ex vivo culture of the endometria alone can be sustained under optimized conditions.

Regarding the device settings, while establishing the final setting preferring upright microscopes, we have also developed an inverted PDMS-bottom setting (Supplementary Fig. 1A). Optimizations of the setting might enable long-term live imaging of implantation and embryogenesis under inverted microscopes. This may propose an advanced platform for dynamic visualization of implantation and developmental processes with cutting-edge imaging technologies<sup>72</sup>.

In addition, our system has significant potential for human applications. For example, primary endometrial tissue cultures derived from patients with implantation disorders would constitute a defective

implantation model ex vivo. This approach is feasible because endometrial biopsies are already routinely performed in IVF clinics as part of implantation failure assessments. Moreover, endometrial tissues from women without implantation disorders can be obtained from benign gynecological surgery specimens, ensuring the applicability of the system to human research, in combination with high-throughput chemical library screening technologies<sup>73,74</sup>.

Within the embryo research field, the clinical data underscores the significance of implantation research. Implantation remains the most significant bottleneck in infertility treatments. Therefore, understanding the molecular mechanisms underlying embryo-uterine interactions is essential for developing effective interventions. By advancing research on implantation-specific processes, our system provides critical steps toward addressing human implantation failure and developing targeted therapeutic strategies.

## Methods

### Ethics

Every experiment has been carried out following a protocol approved by an ethical commission.

### Animals

All mice were housed under specific-pathogen-free conditions with ad libitum feeding under a controlled environment (20–26 °C, 40–70% humidity, 12-h light/dark cycle, lights on at 8 AM). All experiments were approved by the Institutional Animal Care and Use Committee of Osaka University in compliance with relevant guidelines and regulations. In this study, all experiments except blastocyst transfer used wild-type B6D2F1/J females. For blastocyst transfer, wild-type ICR females were used. All B6D2F1/J and ICR females were purchased from Japan SLC. Females were mated with males carrying RBGS<sup>75</sup> or Gt(ROSA)26Sor<sup>tm4(AC1TB-tdTomato,-EGFP)Lo</sup> (mTmG) transgenes<sup>76</sup> with B6D2F1/J background, expressing DsRed2 or tdTomato in the mitochondria or cell membrane, respectively, of all embryonic/extraembryonic cell lineages. mTmG mice were purchased from The Jackson Laboratory (Bar Harbor, ME, USA). All female mice used were between 2 and 4 months old, and all male mice used were between 2 and 6 months old.

### Co-culture system

**Culture media.** For the co-culture system, the ex vivo implantation medium (EXiM) based on the IVC2 medium<sup>11</sup> was defined, composed of the following: Advanced DMEM/F12 (12634010, Thermo Fisher Scientific, USA) supplemented with 30% (vol/vol) KSR (10828028, Thermo Fisher Scientific, USA), ITS-X (094-06761, Fuji film, Japan), GlutaMAX Supplement (35050061, Thermo Fisher Scientific, USA), 3 pg/mL 17- $\beta$  estradiol (14541-74, Nacalai Tesque, Japan), 60 ng/mL progesterone (28921-51, Nacalaitesque, Japan), and penicillin-streptomycin



(10378–016, Thermo Fisher Scientific, USA). For long operations outside the incubator, the 0.476% (wt/vol) HEPES-containing EXiM medium (HEXiM) was used. For the assessment of the effect of FBS, 30% KSR was replaced with 20% (vol/vol) or 30% (vol/vol) FBS (F7524 Lot: BCBW1150 and Lot: 0001653235, Sigma-Aldrich, USA) as appropriate. For inhibitor experiments, 30  $\mu$ M celecoxib (S1261, Selleck, US) and 10  $\mu$ M and 100  $\mu$ M MK-2206 2HCl (S1078, Selleck, US) were administered from the beginning of the co-culture.

**Agarose gel preparation.** 1.5% (wt/vol) SeaKem Gold Agarose (50152, Lonza, Switzerland) was suspended with 33 ml ultrapure water in a 10 dish with 2 mm wide, 3 mm long, and 1 mm high PDMS fragments as molds for the gel spots in which samples were transferred after 24 h. The gel was cut for each experiment and set in a 35 mm plastic bottom dish (1000-035, IWAKI, JAPAN). Before mouse tissue collection, the EXiM medium was equilibrated in the gel three times in a CO<sub>2</sub> incubator.

**Isolation of the recipient endometria.** The day of the vaginal plug confirmation (10 am) was defined as E0.5 for embryos and days post coitum 0.5 (dpc 0.5) for mothers. Female mice were humanely sacrificed by cervical dislocation at dpc 3.75 (4 pm), and the uteri were harvested. Only the uteri from which blastocysts were obtained from one uterine horn were eligible for the experiment, and the other uterine horn, which was not flushed, was processed for endometrial isolation. Each end of a uterine horn was held by micro bulldog forceps on the lid of a 10 cm dish invertedly set on TOKAI HIT thermoplate at 37 °C. Then, 100  $\mu$ l HEXiM medium was added to the uterine horn, and the uterine wall on the mesometrial side was removed with micro-scissors under a stereomicroscope. Then the boundary between the myometrium and the endometrium was cut and a sheet of endometrium was isolated. The isolated endometrium was then cut into 1.5 × 2.0 mm rectangular fragments for each experiment.

**Placement of embryos.** Fluorescent blastocysts at E3.75 were collected from donor uteri by flushing uterine horns with the HEXiM medium. Both zona-free hatched blastocysts and unhatched blastocysts with zona removal by acidified Tyrode's solution (AT) were used. In the latter case, the exposure duration to AT was tried to be mitigated. Obtained blastocysts were temporarily stored in HEXiM drops covered by liquid paraffin until the end of the endometrial isolation procedure. After the preparation of embryos and endometrial fragments, each endometrial fragment was placed on a 1.5% agarose gel and one to three blastocysts were placed on each endometrial fragment with a glass capillary. To prevent liquid paraffin contamination, blastocysts were washed three times with EXiM drops before loading. After the placement of embryos, the samples were covered with originally manufactured ceilings of PDMS (SILPOT 184, DuPont Toray, Japan). Each PDMS ceiling had a 1 mm-thick vent sculpted with a surgical knife to reduce the inner pressure during the coverage to promote physical contact between the endometria and PDMS ceilings and accelerate medium inflow into the PDMS cavity. For the experiments to verify the effect of the direction of oxygen supply, an originally developed 35 mm PDMS bottom dish in which the bottom of the plastic dish was removed and replaced with 750  $\mu$ m -thick PDMS attached by polyimide double-sided adhesive tape (API-214A, Chukoh, Japan), and a porous membrane (TCTP02500, Merck Millipore, USA) connected to Kapton tape (an overlay of 760H#25, TERAOKA, Japan and P-223, Nitto America, USA) with an 8 mm diameter circular hole were used to fix the endometrium and embryos. For the experiments of differential oxygen gas-exchange efficiencies, 50/250/1500  $\mu$ m-thick PDMS were used, and for a highly hypoxic condition, 150  $\mu$ m-thick glasses (CO18181, Matsunami, Japan) with 250  $\mu$ m-thick PDMS frames were placed on the endometria. For embryonic sole culture, a plastic bottom dish (1000-035, IWAKI, Japan) was used for liquid phase conditions and a PDMS-bottom dish was used for aerial phase conditions.

**PDMS removal and sample transfer.** At 24 h, PDMS ceilings were uncovered to assess the embryonic attachment, and the samples were immediately transferred to the neighboring rectangular spots with a width of 2 mm, a length of 3 mm, and a depth of 1 mm. If the endometria adhered to PDMS ceilings, they were removed immediately above the spots by hooking them at the edge of the spots with gentle vertical pressure over the ceilings with forceps and slight horizontal movement to drop the endometria into the spots. Afterward, samples were observed at 48 h and 96 h to evaluate the sustention or shedding of embryos.

**Judgment of embryonic attachment.** Embryonic attachment at 24 h after PDMS removal was defined as adhesion so robust that the embryos did not move away even after a couple of blows with a glass capillary strong enough to move the endometrium. While most unattached embryos immediately fell off upon PDMS removal, some embryos faintly adhered to the endometria right after PDMS removal but were spontaneously shed after the transfer to the spots or easily detached with the blows from a glass capillary. These cases were determined as “unattached”.

### Myr-AKT1-AAV1 construction and transfection experiments

The original vector construct of the myristoylation signal-attached AKT1 (myr-AKT1)<sup>52</sup> was purchased from Addgene (#49186, USA). The target sequence was excised with restriction enzymes and replaced with the EGFP sequence in the pscAAV-CAG-EGFP vector purchased from Addgene (#83279, USA). Then, the pscAAV-CAG-myr-AKT1 vector was co-incubated with HEK293T cells using a *rep/cap* vector for AAV1 (gift from University of Pennsylvania) and pHelper Vector in AAVpro Helper Free System (Takara, Japan) with calcium phosphate to produce myr-AKT1-AAV1 with CAG promoter. HEK293T cells were cultured in DMEM (11995–065, Thermo Fisher Scientific, USA) supplemented with 10% fetal bovine serum and 1% Penicillin-Streptomycin-Glutamine (10378–016, Thermo Fisher Scientific, USA) at 37 °C under 5% CO<sub>2</sub> in air. Myr-AKT1-AAV1 was purified with AAVpro Purification Kit (All Serotypes) (6666, Takara Bio, Japan) and concentrated in PBS. The titer was measured by quantitative PCR with AAVpro Titration Kit (for Real Time PCR) Ver.2 (6233, Takara Bio, Japan). The myr-AKT1-AAV1 stock solution was stored at –80 °C and after thawing it was added to EXiM medium at a concentration of 1 × 10<sup>10</sup> vg/mL. In vitro fertilization (IVF)-derived embryos were frozen-thawed and cultured in KSOM medium for 4 days and blastocyst-stage embryos were incubated in myr-AKT1-AAV1-containing KSOM drops covered by liquid paraffin on a plastic bottom dish in a 37 °C CO<sub>2</sub> incubator for 6 h. Then the embryos were washed three times in KSOM drops and used for ex vivo co-culture or blastocyst transfer in pseudopregnant mice.

### Blastocyst transfer

Following a previous report<sup>42</sup>, celecoxib was suspended in 0.5% (wt/vol) methylcellulose and 0.1% (vol/vol) polysorbate 80 dissolved in water by constant stirring and was given by oral gavage. 300 mg/kg celecoxib was orally administered twice a day to pseudopregnant ICR mice in the morning and evening from dpc 0.75 to dpc 4.75. The myr-AKT1-AAV1-treated embryos were transferred at E2.75 (4 pm), with 16 embryos transferred per mouse with 8 embryos in each uterine horn. Then implantation sites were assessed at dpc 5.5 after intravenous injection of 1% solution of Chicago sky blue 6B (C8679, Sigma-Aldrich, USA) in saline.

### Single-cell RNA-sequencing

For embryonic scRNA-seq, E4.5 in vivo embryos and 24 h ex vivo embryos were microscopically isolated, immediately soaked in Accu-max (17087-54, Nacalai Tesque, Japan) at room temperature, and dissociated with glass capillaries. The capillaries were sequentially

changed from thicker to thinner ones, and only dispersed single cells were manually picked up into 0.04% BSA (wt/vol) in PBS(-). The single-cell suspension from a total of 33 *in vivo* embryos at E4.5 from 4 mice and 32 *ex vivo* embryos at 24 h from 4 donor mice was immediately processed for RNA sequencing library preparation using Chromium Next GEM Single Cell 3' Library and Gel Bead Kit v3.1 (PN-1000268, 10x genomics, USA), Chromium Next GEM Chip G Single Cell Kit (PN-1000120, 10x genomics, USA), and Chromium iX (10x genomics, USA). Then, paired-end sequencing was performed on a next-generation sequencer NovaSeq X Plus (Illumina, USA).

For endometrial scRNA-seq, the 10x Genomics Gene Expression Flex protocol was employed. Dpc 4.5 uterine lumen was gently flushed with 10% neutral buffered formalin (NBF) (37152-51, Nacalai Tesque, Japan) immediately after sacrifice, and implantation sites (ISs) and inter-implantation sites (I-ISs) were microscopically excised into ~500  $\mu$ m size. Finally, 66 ISs and 70 I-ISs from 7 mice were isolated. Similarly, 24 h *ex vivo* ISs and I-ISs were microscopically collected after 10% NBF fixation. A total of 56 ISs and 81 I-ISs from 3 recipient mice were obtained. Isolated samples were processed using Chromium Next GEM Single Cell Fixed RNA Sample Preparation Kit (PN-1000414, 10x genomics, USA), and tissue dissociation was performed with Liberase TL (05401020001, Roche, Switzerland) in RPMI1640 (11875093, Thermo Fisher Scientific, USA) using gentleMACS Octo Dissociator with Heaters (Miltenyi Biotech, Germany). After cell counting, the single-cell suspension was treated for RNA sequencing library preparation with Chromium Fixed RNA Kit, Mouse Transcriptome (PN-1000496, 10x genomics, USA), Chromium Mouse Transcriptome Probe Set v1.0.1 (10x genomics, USA), and Chromium X (10x genomics, USA). Then, paired-end sequencing was performed on an Illumina next-generation sequencer NovaSeq X Plus (Illumina, USA).

The raw fastq files were processed by the software Cell Ranger v7.2(10x genomics, USA) and Seurat (<http://www.satijalab.org/seurat>)<sup>77</sup> v5.0.0 was then used to process the read counts. CellChat v2<sup>78</sup> was used for the cell-cell interaction assay. To perform Gene Ontology (GO) enrichment analysis, a modified Fisher's exact test was used.

### Bulk RNA sequencing

Solely cultured or co-cultured *ex vivo* embryos with or without celecoxib treatment were collected at 24 h. Embryos were immediately dissolved in SMART-Seq HT Kit 10X Lysis Buffer (635013, Takara Bio, Japan) and processed for RNA sequencing library preparation. 6 embryos per animal were integrated as one biological replicate, and 3/3/2 biological replicates for sole-culture with DMSO/sole-culture with celecoxib/co-culture with DMSO/co-culture with celecoxib *ex vivo* and were investigated and 3 biological replicates were examined for e4.5 *in vivo* embryos in vehicle and celecoxib groups respectively. For endometrial samples, 3 *ex vivo* ISs in each group from a recipient mouse were cut with micro scissors in 500  $\mu$ m size and combined as one biological replicate. 3 biological replicates for each group were examined. RNA was extracted with TRIzol RNA Isolation Reagents (15596018, Thermo Fisher Scientific, USA). RNA sequencing library was prepared using SMART-Seq mRNA HT LP (634792, TAKARA Bio, Japan). Paired-end sequencing was performed by NovaSeq 6000 (Illumina, USA) and the raw fastq files were analyzed by RaNA-seq (<https://ranaseq.eu/>) v1.0 and Metascape (<https://metascape.org/gp/index.html>) v3.5.20250101. In Fig. 6A, DEGs were automatically calculated from fastq files by RaNA-seq, using DESeq2 Wald test with a *P* value cutoff 0.05. Enrichment analysis for downregulated DEGs was performed using Metascape. GSEA analysis was performed on RaNA-seq.

### Histology

Frozen samples were cut into 10  $\mu$ m sections with a cryostat and processed for immunofluorescence or H&E staining. The sections were observed under an Olympus BX-53 microscope (Tokyo, Japan).

### Immunofluorescence

For CK8 and COX-2 immunofluorescence, 10  $\mu$ m-thick fixed-frozen sections were permeabilized with 0.2% PBST. After blocking with 1% BSA/PBST, slides were incubated with the anti-CK8 antibody (1:1000, rat, AB531826, DSHB, USA) and anti-COX-2 antibody (1:300, rabbit, AA570-598, Cayman, USA) in 1% BSA/PBST overnight at 4 °C. After washing with PBST, slides were incubated with Alexa Fluor 647-conjugated goat anti-mouse IgG (1:300, A21235, Invitrogen, USA) and Alexa Fluor 488-conjugated goat anti-rabbit IgG (1:300, A11070, Invitrogen, USA), and Hoechst33342 (H3570, Invitrogen, USA, 1:3000) in 1% BSA/PBST for 1 h at room temperature. After washing, sections were mounted with Immu-Mount (9990402, epreidia, USA) and photographed with an Olympus BX-53 microscope (Tokyo, Japan) or a Nikon eclipse Ti microscope (Nikon, Japan). COX-2 positive area was analyzed by the software ImageJ<sup>79</sup>. For pAKT and AKT immunofluorescence on histological sections, anti-pAKT (1:300, rabbit, #4060, Cell Signaling, USA), different from the whole-mount staining below, and anti-AKT (1:300, mouse, #2920, Cell Signaling, USA) were used. For AKT and CK8 staining, sequential sections were used because of the significant overlap in the same section.

### Whole-mount Immunofluorescence

Samples were briefly fixed with 10% NBF for 15 minutes at room temperature to avoid desensitizing the fluorescent signal of DsRed2 or tdTomato. For OCT4 and CDX2 immunofluorescence, samples were permeabilized with 0.2% PBST. After blocking with 1% BSA/PBST, samples were incubated with the anti-OCT4 (1:300, rabbit, PM048, MBL, Japan) and anti-CDX2 (1:300, mouse, MU392-UC, Biogenex, USA) antibodies in 1% BSA/PBST overnight at 4 °C. After washing with PBST, samples were incubated with Alexa Fluor 488-conjugated goat anti-rabbit IgG (1:300, A11070, Invitrogen, USA), Alexa Fluor 647-conjugated goat anti-mouse IgG (1:300, A21235, Invitrogen, USA), and Hoechst33342 (H3570, Invitrogen, USA, 1:3000) in 1% BSA/PBST for 1 h at room temperature. For FOXA2 and CDX2 immunofluorescence, anti-FOXA2 (1:300, rabbit, #8186, Cell Signaling, USA) antibody was used with the same protocol as OCT4/CDX2 staining. For pAKT and AKT, 2% PBST was used for permeabilization, and anti-pAKT (Ser473, pan) (1:300, rabbit, #4058, Cell Signaling, USA) and anti-AKT (pan) (1:300, mouse, #2920, Cell Signaling, USA) were used for the primary antibodies, and Alexa Fluor 488-conjugated goat anti-mouse IgG (1:300, A11017, Invitrogen, USA), Alexa Fluor 647-conjugated goat anti-rabbit IgG (1:300, A21245, Invitrogen, USA) for the secondary antibodies. For CD45, F4/80, KLF5,  $\alpha$ SMA, FLK-1, Ki67, and E-cadherin, primary antibodies for CD45 (1:300, rat, #103101, BioLegend, USA), F4/80 (1:300, rat, MCA497, BIORAD), KLF5 (1:300, rabbit, #21017-1-AP, Proteintec, USA),  $\alpha$ SMA (1:300, rabbit, #19245, Cell Signaling, USA), FLK-1 (1:300, rat, #550549, BD Biosciences, USA), Ki67 (1:300, rabbit, MAS-14520, Thermo Fisher Scientific, USA), and E-cadherin (1:300, rabbit, #3195, Cell Signaling, USA) were used with the appropriate secondary antibodies with the same protocol as pAKT/AKT staining. See Supplementary Table 4A and B for the specific antibody information. After washing, samples were cleared and mounted in RapiClear 1.47 (RC147001, SUNJin Lab, Taiwan) with iSpacer (ISO17, SUNJin Lab, Taiwan) on a 35 mm glass bottom dish (P35G-1.5-14/C/H, MATTEK, USA). Three-dimensional images were obtained with a confocal microscope AX R with NSPARC (Nikon, Japan) using a 25x silicone immersion objective lens at 0.5  $\mu$ m-each distance in the Z axis.

For imaging analysis, Imaris (version 10.1.0, Oxford Instruments, UK) was used. Imaris automatically calculated the mean intensity per voxel for each embryonic region for three-dimensional quantification of pAKT and AKT immunofluorescence. The calculation of embryonic invasion volume was obtained using the following criteria: In a series of vertical slices of a three-dimensional confocal image, the putative endometrial surface line breached by the embryos was manually drawn on Imaris by smoothly connecting the surface of the endometrium

around the embryo. By connecting this line with the line that encloses the embryo protruding outside the endometrium, Imaris automatically created a smooth three-dimensional surface. After omitting the embryonic part outside the endometrium using the surface, Imaris automatically calculated the volume of the embryonic part below the surface.

### Statistical analysis

Statistical analyses were performed using a two-tailed Student's t-test or one-way ANOVA followed by Tukey post-hoc tests on GraphPad Prism 9.2.0 (MDF, Japan) as appropriate. Statistical significance was set at *P* value less than 0.05.

### Data presentation

All graph presentation was performed with GraphPad Prism 9.2.0 (MDF, Japan).

### Reporting summary

Further information on research design is available in the Nature Portfolio Reporting Summary linked to this article.

### Data availability

All data supporting the findings of this study are available within the article and its supplementary files. Any additional requests for information can be directed to, and will be fulfilled by, the corresponding authors. Source data are provided with this paper. The raw and processed bulk RNA-seq or scRNA-seq data are available in the NCBI Gene Expression Omnibus (GEO) under accession numbers GSE279808 and GSE279809 (scRNA-seq) and GSE279268 (bulk RNA-seq). Source data are provided with this paper.

### References

- Glujovsky, D. et al. Cleavage-stage versus blastocyst-stage embryo transfer in assisted reproductive technology. *Cochrane Database Syst. Rev.* **5**, CD002118 (2022).
- Quenby, S. et al. Miscarriage matters: the epidemiological, physical, psychological, and economic costs of early pregnancy loss. *Lancet* **397**, 1658–1667 (2021).
- Shapiro, B. S. et al. Evidence of impaired endometrial receptivity after ovarian stimulation for in vitro fertilization: a prospective randomized trial comparing fresh and frozen-thawed embryo transfer in normal responders. *Fertil. Steril.* **96**, 344–348 (2011).
- Takeda, K. et al. Targeted disruption of the mouse Stat3 gene leads to early embryonic lethality. *Proc. Natl Acad. Sci. USA* **94**, 3801–3804 (1997).
- Ohtani, T. et al. Dissection of signaling cascades through gp130 in vivo: reciprocal roles for STAT3- and SHP2-mediated signals in immune responses. *Immunity* **12**, 95–105 (2000).
- Ware, C. B. et al. Targeted disruption of the low-affinity leukemia inhibitory factor receptor gene causes placental, skeletal, neural and metabolic defects and results in perinatal death. *Development* **121**, 1283–1299 (1995).
- Lydon, J. P. et al. Mice lacking progesterone receptor exhibit pleiotropic reproductive abnormalities. *Genes Dev.* **9**, 2266–2278 (1995).
- Sun, X., Bartos, A., Whitsett, J. A. & Dey, S. K. Uterine deletion of Gp130 or Stat3 shows implantation failure with increased estrogenic responses. *Mol. Endocrinol.* **27**, 1492–1501 (2013).
- Hiraoka, T. et al. Differential roles of uterine epithelial and stromal STAT3 coordinate uterine receptivity and embryo attachment. *Sci. Rep.* **10**, 15523 (2020).
- Fukui, Y. et al. Uterine epithelial LIF receptors contribute to implantation chamber formation in blastocyst attachment. *Endocrinology* **162**, bqab169 (2021).
- Bedzhov, I., Leung, C. Y., Bialecka, M. & Zernicka-Goetz, M. In vitro culture of mouse blastocysts beyond the implantation stages. *Nat. Protoc.* **9**, 2732–2739 (2014).
- Aguilera-Castrejon, A. et al. Ex utero mouse embryogenesis from pre-gastrulation to late organogenesis. *Nature* **593**, 119–124 (2021).
- Amadei, G. et al. Embryo model completes gastrulation to neurulation and organogenesis. *Nature* **610**, 143–153 (2022).
- Kagawa, H. et al. Human blastoids model blastocyst development and implantation. *Nature* **601**, 600–605 (2022).
- Tarazi, S. et al. Post-gastrulation synthetic embryos generated ex utero from mouse naive ESCs. *Cell* **185**, 3290–3306.e3225 (2022).
- Yu, L. et al. Blastocyst-like structures generated from human pluripotent stem cells. *Nature* **591**, 620–626 (2021).
- Liu, L. et al. Modeling post-implantation stages of human development into early organogenesis with stem-cell-derived perigastruloids. *Cell* **186**, 3776–3792.e3716 (2023).
- Oldak, B. et al. Complete human day 14 post-implantation embryo models from naive ES cells. *Nature* **622**, 562–573 (2023).
- Weatherbee, B. A. T. et al. Pluripotent stem cell-derived model of the post-implantation human embryo. *Nature* **622**, 584–593 (2023).
- Govindasamy, N. et al. 3D biomimetic platform reveals the first interactions of the embryo and the maternal blood vessels. *Dev. Cell* **56**, 3276–3287.e3278 (2021).
- Bondarenko, V. et al. Embryo-uterine interaction coordinates mouse embryogenesis during implantation. *EMBO J.* **42**, e113280 (2023).
- Shibata, S. et al. Modeling embryo-endometrial interface recapitulating human embryo implantation. *Sci. Adv.* **10**, eadi4819 (2024).
- Sato, T. et al. In vitro production of functional sperm in cultured neonatal mouse testes. *Nature* **471**, 504–507 (2011).
- Kamoshita, M. et al. Development of the membrane ceiling method for in vitro spermatogenesis. *Sci. Rep.* **15**, 625 (2025).
- Nilsson, M. E. et al. Measurement of a comprehensive sex steroid profile in rodent serum by high-sensitive gas chromatography-tandem mass spectrometry. *Endocrinology* **156**, 2492–2502 (2015).
- Cha, J., Sun, X. & Dey, S. K. Mechanisms of implantation: strategies for successful pregnancy. *Nat. Med.* **18**, 1754–1767 (2012).
- Li, Y., Sun, X. & Dey, S. K. Entosis allows timely elimination of the luminal epithelial barrier for embryo implantation. *Cell Rep.* **11**, 358–365 (2015).
- Akaeda, S. et al. Retinoblastoma protein promotes uterine epithelial cell cycle arrest and necroptosis for embryo invasion. *EMBO Rep.* **22**, e50927 (2021).
- Christodoulou, N. et al. Morphogenesis of extra-embryonic tissues directs the remodelling of the mouse embryo at implantation. *Nat. Commun.* **10**, 3557 (2019).
- Suzuki, D., Sasaki, K., Kumamoto, S., Tanaka, K. & Ogawa, H. Dynamic changes of gene expression in mouse mural trophoblast regulated by Cdx2 during implantation. *Front Cell Dev. Biol.* **10**, 945241 (2022).
- Yu, L. et al. Large-scale production of human blastoids amenable to modeling blastocyst development and maternal-fetal cross talk. *Cell Stem Cell* **30**, 1246–1261.e1249 (2023).
- Liu, D. et al. Primary specification of blastocyst trophectoderm by scRNA-seq: New insights into embryo implantation. *Sci. Adv.* **8**, eabj3725 (2022).
- Sun, X. et al. Kruppel-like factor 5 (KLF5) is critical for conferring uterine receptivity to implantation. *Proc. Natl Acad. Sci. USA* **109**, 1145–1150 (2012).
- Li, R. et al. Spatial transcriptomic profiles of mouse uterine microenvironments at pregnancy day 7.5. *Dev. Biol.* **107**, 529–545 (2022).
- Matsumoto, H. & Sato, E. Uterine angiogenesis during implantation and decidualization in mice. *Reprod. Med. Biol.* **5**, 81–86 (2006).



36. Yuan, J. et al. Primary decidual zone formation requires Scribble for pregnancy success in mice. *Nat. Commun.* **10**, 5425 (2019).
37. Aikawa, S. & Hirota, Y. Roles of lipid mediators in early pregnancy events. *Reprod. Med. Biol.* **23**, e12597 (2024).
38. Fukui, Y. et al. Uterine receptivity, embryo attachment, and embryo invasion: Multistep processes in embryo implantation. *Reprod. Med. Biol.* **18**, 234–240 (2019).
39. Jiang, X. et al. A differentiation roadmap of murine placentation at single-cell resolution. *Cell Discov.* **9**, 30 (2023).
40. Ozguldez, H. O. et al. Polarity inversion reorganizes the stem cell compartment of the trophoblast lineage. *Cell Rep.* **42**, 112313 (2023).
41. Lim, H. et al. Multiple female reproductive failures in cyclooxygenase 2-deficient mice. *Cell* **91**, 197–208 (1997).
42. Reese, J. et al. Comparative analysis of pharmacologic and/or genetic disruption of cyclooxygenase-1 and cyclooxygenase-2 function in female reproduction in mice. *Endocrinology* **142**, 3198–3206 (2001).
43. Aikawa, S. et al. Spatiotemporally distinct roles of cyclooxygenase-1 and cyclooxygenase-2 at feto-maternal interface in mice. *JCI insight*, **9**, e181865 (2024).
44. Wang, H. Q. et al. Maternal and embryonic signals cause functional differentiation of luminal epithelial cells and receptivity establishment. *Dev. Cell* **58**, 2376–2392 e2376 (2023).
45. Dinchuk, J. E. et al. Renal abnormalities and an altered inflammatory response in mice lacking cyclooxygenase II. *Nature* **378**, 406–409 (1995).
46. Matsumoto, L. et al. HIF2 $\alpha$  in the uterine stroma permits embryo invasion and luminal epithelium detachment. *J. Clin. Invest* **128**, 3186–3197 (2018).
47. Manning, B. D. & Toker, A. AKT/PKB Signaling: Navigating the Network. *Cell* **169**, 381–405 (2017).
48. Chen, W. S. et al. Growth retardation and increased apoptosis in mice with homozygous disruption of the Akt1 gene. *Genes Dev.* **15**, 2203–2208 (2001).
49. Cho, H., Thorvaldsen, J. L., Chu, Q., Feng, F. & Birnbaum, M. J. Akt1/PKB $\alpha$  is required for normal growth but dispensable for maintenance of glucose homeostasis in mice. *J. Biol. Chem.* **276**, 38349–38352 (2001).
50. Yang, Z. Z. et al. Protein kinase B  $\alpha$ /Akt1 regulates placental development and fetal growth. *J. Biol. Chem.* **278**, 32124–32131 (2003).
51. Yang, Z. Z. et al. Dosage-dependent effects of Akt1/protein kinase B  $\alpha$  (PKB $\alpha$ ) and Akt3/PKB $\gamma$  on thymus, skin, and cardiovascular and nervous system development in mice. *Mol. Cell Biol.* **25**, 10407–10418 (2005).
52. Aoki, M., Batista, O., Bellacosa, A., Tsichlis, P. & Vogt, P. K. The akt kinase: molecular determinants of oncogenicity. *Proc. Natl Acad. Sci. USA* **95**, 14950–14955 (1998).
53. Aikawa, S. et al. Uterine deficiency of high-mobility group box-1 (HMGB1) protein causes implantation defects and adverse pregnancy outcomes. *Cell Death Differ.* **27**, 1489–1504 (2020).
54. Ono, Y. et al. CD206<sup>+</sup> M2-Like Macrophages Are Essential for Successful Implantation. *Front Immunol.* **11**, 557184 (2020).
55. Sanjo, H. et al. Antioxidant vitamins and lysophospholipids are critical for inducing mouse spermatogenesis under organ culture conditions. *FASEB J.* **34**, 9480–9497 (2020).
56. Aikawa, S. et al. Autotaxin-lysophosphatidic acid-LPA(3) signaling at the embryo-epithelial boundary controls decidualization pathways. *EMBO J.* **36**, 2146–2160 (2017).
57. Akaeda, S., Aikawa, S. & Hirota, Y. Spatial and molecular anatomy of the endometrium during embryo implantation: a current overview of key regulators of blastocyst invasion. *FEBS J.* <https://doi.org/10.1111/febs.17077> (2024).
58. Haraguchi, H. et al. MicroRNA-200a locally attenuates progesterone signaling in the cervix, preventing embryo implantation. *Mol. Endocrinol.* **28**, 1108–1117 (2014).
59. Kim, M. et al. VEGF-A regulated by progesterone governs uterine angiogenesis and vascular remodelling during pregnancy. *EMBO Mol. Med.* **5**, 1415–1430 (2013).
60. Song, M., Bode, A. M., Dong, Z. & Lee, M. H. AKT as a Therapeutic Target for Cancer. *Cancer Res.* **79**, 1019–1031 (2019).
61. Segi, E. et al. Patent ductus arteriosus and neonatal death in prostaglandin receptor EP4-deficient mice. *Biochem Biophys. Res. Commun.* **246**, 7–12 (1998).
62. Tilley, S. L. et al. Reproductive failure and reduced blood pressure in mice lacking the EP2 prostaglandin E2 receptor. *J. Clin. Invest* **103**, 1539–1545 (1999).
63. Matsuoka, T. et al. Prostaglandin D2 as a mediator of allergic asthma. *Science* **287**, 2013–2017 (2000).
64. Sugimoto, Y. & Narumiya, S. Prostaglandin E receptors. *J. Biol. Chem.* **282**, 11613–11617 (2007).
65. Sakamoto, R. et al., Uterine prostaglandin DP receptor induced upon implantation contributes to decidualization together with EP4 receptor. *J. Lipid Res.* **65**, 100636 (2024).
66. Dormond, O., Foletti, A., Paroz, C. & Ruegg, C. NSAIDs inhibit  $\alpha$  V  $\beta$  3 integrin-mediated and Cdc42/Rac-dependent endothelial-cell spreading, migration and angiogenesis. *Nat. Med.* **7**, 1041–1047 (2001).
67. Liu, J. F. et al. Cyclooxygenase-2 enhances  $\alpha$ 2 $\beta$ 1 integrin expression and cell migration via EP1 dependent signaling pathway in human chondrosarcoma cells. *Mol. Cancer* **9**, 43 (2010).
68. Li, C. & Samulski, R. J. Engineering adeno-associated virus vectors for gene therapy. *Nat. Rev. Genet.* **21**, 255–272 (2020).
69. Wang, D., Tai, P. W. L. & Gao, G. Adeno-associated virus vector as a platform for gene therapy delivery. *Nat. Rev. Drug Discov.* **18**, 358–378 (2019).
70. Mizuno, N. et al. Intra-embryo gene cassette knockin by CRISPR/Cas9-mediated genome editing with adeno-associated viral vector. *iScience* **9**, 286–297 (2018).
71. Nakagawa, T., Emori, C., Ikawa, M. Trophectoderm-specific gene manipulation using adeno-associated viral vectors. *Exp Anim*, <https://doi.org/10.1538/expanim.24-0165> (2025).
72. Savolainen, A. et al. 3DMOUSEneST: a volumetric label-free imaging method evaluating embryo-uterine interaction and decidualization efficacy. *Development* **151**, dev202938 (2024).
73. Madasu, C. et al. Identification of potent pan-ephrin receptor kinase inhibitors using DNA-encoded chemistry technology. *Proc. Natl Acad. Sci. USA* **121**, e2322934121 (2024).
74. Jimmidi, R. et al. Discovery of highly potent and ALK2/ALK1 selective kinase inhibitors using DNA-encoded chemistry technology. *Proc. Natl Acad. Sci. USA* **121**, e2413108121 (2024).
75. Hasuwa, H. et al. Transgenic mouse sperm that have green acrosome and red mitochondria allow visualization of sperm and their acrosome reaction in vivo. *Exp. Anim.* **59**, 105–107 (2010).
76. Muzumdar, M. D., Tasic, B., Miyamichi, K., Li, L. & Luo, L. A global double-fluorescent Cre reporter mouse. *Genesis* **45**, 593–605 (2007).
77. Hao, Y. et al. Dictionary learning for integrative, multimodal and scalable single-cell analysis. *Nat. Biotechnol.* **42**, 293–304 (2024).
78. Jin, S. et al. Inference and analysis of cell-cell communication using CellChat. *Nat. Commun.* **12**, 1088 (2021).
79. Schneider, C. A., Rasband, W. S. & Eliceiri, K. W. NIH Image to ImageJ: 25 years of image analysis. *Nat. Methods* **9**, 671–675 (2012).

## Acknowledgements

This paper was supported by the following grants: Japan Society for the Promotion of Science (JSPS) grants, JP23K15814 to T.H., JP23K27176 to S.A., JP23K23803 to Y.H., and JP21H05033, JP22H04922, JP23K20043,

25H01353 to M.I. Japan Science and Technology Agency (JST) grants, JPMJFR210H to S.A. and JPMJCR21N1 to H.K. and M.I. Astellas Foundation for Research on Metabolic Disorders to S.A. The Naito Foundation to S.A. Children and Families Agency grant, JPMH23DB0101 to Y.H. Japan Agency for Medical Research and Development (AMED) grants, JP24gn0110069 to Y.H. and JP23jf0126001, JP223fa627002, and JP223fa627006 to M.I. The authors are grateful to Dr. James M. Wilson at the University of Pennsylvania for kindly providing a rep/cap vector for AAV1. The authors would like to thank the Nikon Imaging Center at Osaka University for imaging equipment and software, and the NGS core facility at the Research Institute for Microbial Diseases in Osaka University for scRNA-seq and RNA-seq library preparation. We also thank the members of both the Department of Experimental Genome Research and the nonprofit organization (NPO) for Biotechnology Research and Development for experimental assistance and discussion, especially Ms. Saki Nishioka for blastocyst transfer. This project was promoted by the OU Master Plan Implementation Project under Osaka University.

### Author contributions

T.H. and M.I. designed the study. T.H. performed the experiments and collected and analyzed the data. S.A. and D.M. performed scRNA-seq analysis. T.H. and T.N. developed myr-AKT1-AAV1. H.S. and H.K. manufactured microdevices. T.H., S.A., Y.H., and M.I. discussed and interpreted the results. TH drafted the manuscript, which was edited by S.A. and M.I. Y.H. and H.K. critically reviewed the manuscript. M.I. supervised the study.

### Competing interests

The authors declare no competing interests.

### Additional information

**Supplementary information** The online version contains supplementary material available at <https://doi.org/10.1038/s41467-025-60610-x>.

**Correspondence** and requests for materials should be addressed to Takehiro Hiraoka or Masahito Ikawa.

**Peer review information** *Nature Communications* thanks Jun Wu and the other, anonymous, reviewer(s) for their contribution to the peer review of this work. A peer review file is available.

**Reprints and permissions information** is available at <http://www.nature.com/reprints>

**Publisher's note** Springer Nature remains neutral with regard to jurisdictional claims in published maps and institutional affiliations.

**Open Access** This article is licensed under a Creative Commons Attribution-NonCommercial-NoDerivatives 4.0 International License, which permits any non-commercial use, sharing, distribution and reproduction in any medium or format, as long as you give appropriate credit to the original author(s) and the source, provide a link to the Creative Commons licence, and indicate if you modified the licensed material. You do not have permission under this licence to share adapted material derived from this article or parts of it. The images or other third party material in this article are included in the article's Creative Commons licence, unless indicated otherwise in a credit line to the material. If material is not included in the article's Creative Commons licence and your intended use is not permitted by statutory regulation or exceeds the permitted use, you will need to obtain permission directly from the copyright holder. To view a copy of this licence, visit <http://creativecommons.org/licenses/by-nc-nd/4.0/>.

© The Author(s) 2025